IMPLICATIONS OF THE PORE-SCALE DISTRIBUTION OF FROZEN WATER FOR PRODUCTION OF HYDROCARBON RESERVOIRS LOCATED IN PERMAFROST

By

Kiran Kumar Venepalli

RECOMMENDED:

Advisory Committee Chair

Chair, Department of Petroleum Engineering

APPROVED:

Dean, College of Engineering and Mines

Dean of the Graduate School

August 9, 2011

Date

IMPLICATIONS OF PORE-SCALE DISTRIBUTION OF FROZEN WATER FOR THE PRODUCTION OF HYDROCARBON RESERVOIRS LOCATED IN PERMAFROST

A

THESIS

Presented to the Faculty

of the University of Alaska Fairbanks

in Partial Fulfillment of the Requirements

for the Degree of

MASTER OF SCIENCE

By

Kiran Kumar Venepalli, M.S.

Fairbanks, Alaska

August 2011

Abstract

Frozen reservoirs are unique with the extra element of ice residing in them along with the conventional components of a reservoir. The sub-zero temperatures of these reservoirs make them complicated to explore.

This study investigates reduction in relative permeability to oil with decrease in temperature and proposes a best-production technique for reservoirs occurring in sub zero conditions.

Core flood experiments were performed on two clean Berea sandstone cores under permafrost conditions to determine the sensitivity of the relative permeability to oil (k_{ro}) over a temperature range of 23°C to -10°C and for connate water salinities ranging from 0 to 6467 ppm. Both cores showed maximum reduction in relative permeability to oil when saturated with deionized water; they showed minimum reduction when saturated with 6467 ppm of saline water.

Theoretically, the radius of ice formed in the center of the pore can be determined using the Kozeny–Carman Equation by assuming the pores and pore throats as a cube with 'N' identical parallel pipes embedded in it. With obtained values of k_{ro} as input to the Kozeny–Carman Equation at -10°C, the radius of ice dropped from 0.145 μm to 0.069 μm when flooding–water salinity is increased to 6467 ppm. This analysis quantifies the reductions in relative permeability solely due to different formation salinities. Other parameters like fluid saturations and pore structure effects also are discussed.

Fluids like deionized water, saline water, and antifreeze (a mixture of 60% ethylene or propylene glycol with 40% water) were tested to find the best flooding agent for frozen reservoirs. At 0°C, 9% greater recovery was observed with antifreeze than with saline water. Antifreeze showed 48% recovery even at -10°C, at which temperature the rest of the fluids failed to increase production.

Table of Contents

List of Figures

Page

List of Tables

Page

List of Appendices

Disclaimer

Acknowledgments

First and foremost I would like to thank my advisor, Dr. Jo Mongrain, for her immense support and guidance. She has been truly inspirational. I would also like to take this opportunity to express my gratitude to my committee members, Dr. Shirish Patil, Dr. Catherine Hanks, and Dr. Abhijit Dandekar for their invaluable assistance.

I also wish to thank Melody Hughes, office manager of the Petroleum Engineering Department, for her help regarding administrative requirements.

I extend my sincere thanks to Allen Huckabay, Vijay Bangia, Renaissance Alaska and Mike Dunn, Petro Technical Resources of Alaska, for their constant help in reviewing my research. This material is based upon work supported by the Department of Energy under Award Number DE- FC26-08NT0005641.

Last but not least, I am very grateful to my family and friends. Without their unconditional love and support, this work wouldn't have been possible.

Chapter 1 Introduction

Conventional and unconventional oil are distinguished by measure of API gravity. The transition between conventional and unconventional oil occurs in the range of 10-22^0 API gravity (Figure 1). To date, oil and natural gas industries have focused on producing conventional oil from conventional reservoirs, which are explored using traditional drilling techniques adopted by oil companies. Oil from these reservoirs is recovered either by primary or secondary extraction techniques.

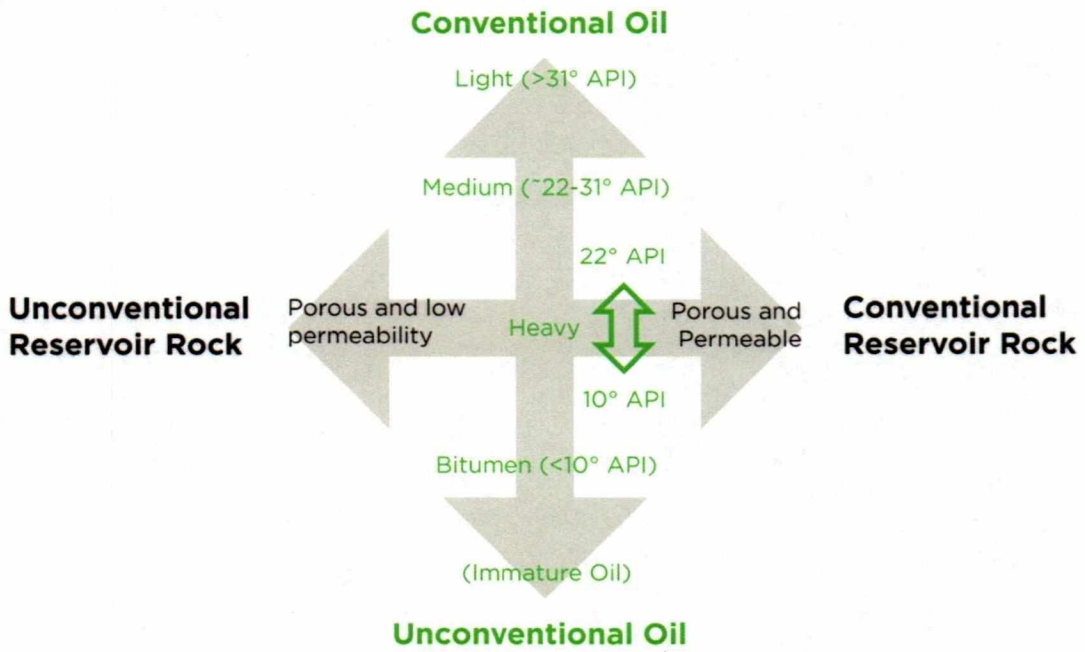

Figure 1: Differentiating conventional oil versus unconventional oil (www.ajmpc.com)

Traditional oil recovery methods from conventional reservoirs are the cheapest, easiest kind of exploration, but conventional oil resources are declining at a rapid rate. The demand for oil in the next few years will overtake the supply of conventional oil (Figure 2). In order to meet projected future demands of society, unconventional resources will need to be tapped. In the next few decades, oil and gas industries are

expected to shift from producing primarily from conventional reservoirs to developing unconventional reservoirs. Indeed, most of the proven oil reserves in the world are found in unconventional sources (Figure 3).

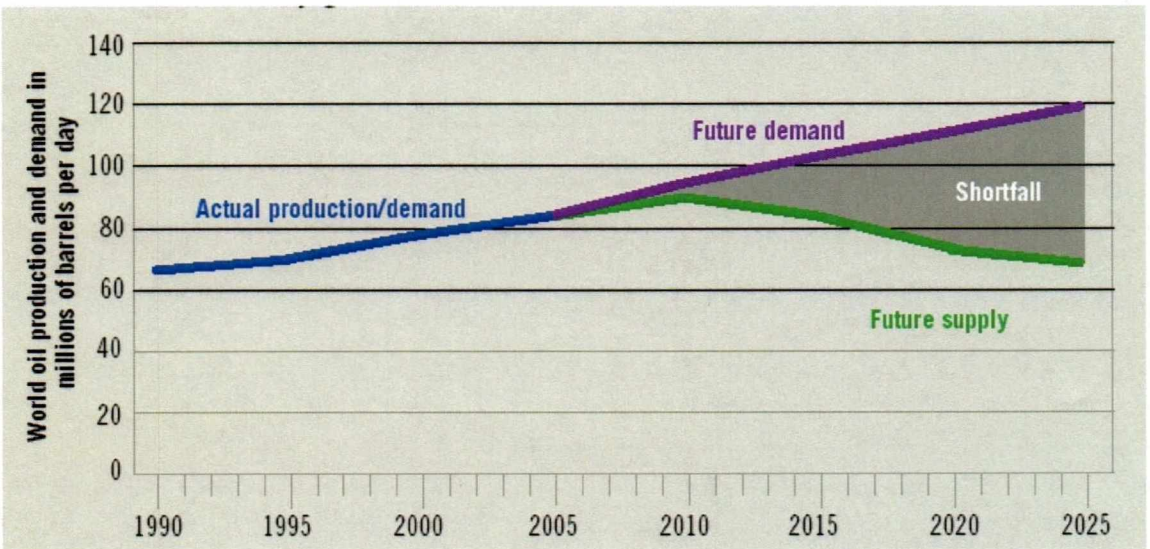

Figure 2: Oil demand and supply forecast (US Energy Information Administration, 2005)

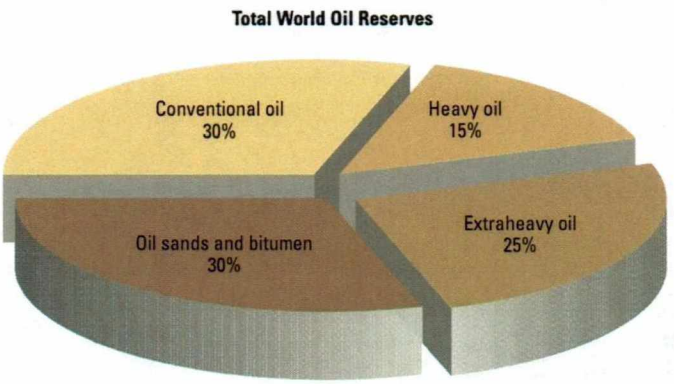

Figure 3: Total world oil reserves (Alboudwarej, 2006)

1.1 Conventional oils in unconventional reservoirs

There exist a difference between conventional oils and conventional reservoirs. Conventional and unconventional oils are distinguished by measure of its API gravity. Light oil (> 31° API) is considered as conventional oil (Figure 1). Bitumen (< 10° API) and immature oils are considered as unconventional oils (Figure 1).

An oil reservoir is typically labeled unconventional when its holdings cannot be recovered using conventional extraction methods. Conventional and unconventional oils may reside in either of the conventional and unconventional reservoirs. The oils and reservoirs are defined in Figure 4.

- **Conventional oil in conventional reservoirs:** The top right quadrant of Figure 4 (green) has been the target of exploration for more than a hundred years and is likely includes the easiest and cheapest ways of exploration
- **Unconventional oil in conventional reservoirs:** The bottom right quadrant of Figure 4 (orange) includes heavy oil and bitumen that require special methods to extract. These oils are more viscous, with low-API gravity and contain heavier components. They are also not as sweet as light oil. They are recovered with enhanced recovery techniques. Typically, they also require extensive refining (Kovarik, 2010).
- **Unconventional oil in unconventional reservoirs:** The bottom left quadrant of Figure 4 (red) would include the oil shales, which require extensive processing like in-situ heating and ex-situ processing through mining.
- **Conventional oil in unconventional reservoirs:** Frozen reservoirs fall into the upper left quadrant of Figure 4 (yellow). These resources typically need special treatment in both drilling and production techniques because of low temperature conditions.

Frozen reservoirs are conventional oils in an unconventional reservoir. The presence of ice along with the other three components (oil, gas, and water) makes frozen reservoirs unique and unconventional to produce. A better understanding of frozen

reservoirs and their development is required in order to advance recovery of oil from them.

Emphasis should be given to frozen reservoirs when developing the technology for producing oil in an economically feasible way, since exploration of other unconventional reserves is relatively expensive and requires even more extensive technology.

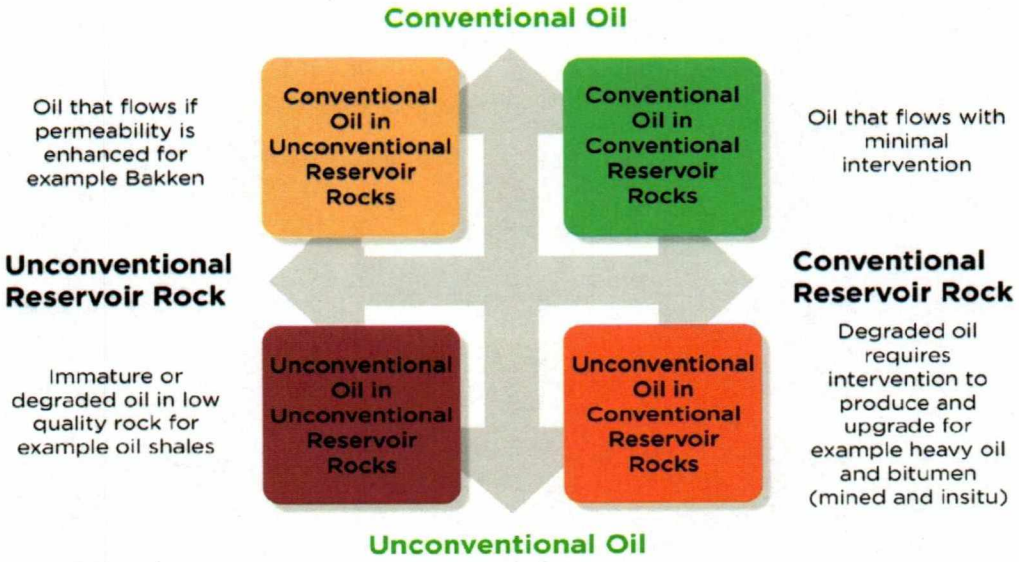

Figure 4: Defining oil and the reservoir (www.ajmpc.com)

1.2 Reservoirs in permafrost and related challenges

The Gubkin gas field (Russia) (Jensen et al., 1983), the northern part of the Timan-Pechora oil and gas field (Russia) (Jensen et al., 1983), and the Umiat oil field (U.S.) (Baptist, 1960) are examples of reservoirs found in permafrost (frozen ground). These reservoirs typically have an extra component of ice along with the conventional reservoir components. Temperatures of less than 0°C can cause problems during drilling and production of these reservoirs.

The freezing of water in drilling fluids can cause problems including lost circulation, stuck pipe, and poor cementing jobs (Kljucec et al., 1974). The effect of temperature also contributes to poor recovery when producing from frozen–ground reservoirs. This is due to the lower values of relative permeability to oil (Baptist, 1960). Baptist (1960) performed several experiments on frozen cores and concluded that low recovery rates resulted from reductions in relative permeability to oil that occurred with drops in temperature from room temperature to below 0°C. He performed experiments only at those two temperatures. However, there was no evidence of change in relative permeability to oil with gradual drops in temperature. Information about the effect of formation water salinity on relative permeability to oil during temperature change in frozen reservoirs is also lacking. Reductions in relative permeability are explained partially by Baptist, who introduced the concept of freezing of interstitial water within pore structure. However, the sensitivity of relative permeability and the structural placement of ice with respect to salinity are unknown. The end result of all of these problems is reduction in productivity. The search for appropriate production mechanisms has evolved due to these challenges. They make it necessary to delve more deeply into frozen reservoirs, with the goal of developing and better understanding their behavior on the micro scale. Thus, this project concentrates on understanding relative permeability to oil behavior with respect to temperature changes as well as to changes in the salinity of formation water. This study also explores several fluid injection strategies as production techniques for frozen reservoirs.

1.3 Objective

The unusual conditions of a frozen reservoir necessitate detailed laboratory study, in order to evaluate the more appropriate production techniques. The effect of temperature on relative permeability is observed at two temperatures, as explained earlier. However, trends of relative permeability over a temperature range of 23°C to -10°C need to be addressed. The effect of salinity on relative permeability to oil also needs

to be determined. Thus, the present study concentrates on pore–scale distribution of water and ice and its effect on relative permeability to oil. Just as important is an investigation of best–production techniques, those that would increase the quantity of "recoverable reserve" in ice-rich reservoirs.

The objectives of this thesis are as follows:

- Build an experimental setup
- Run routine core analysis on two Berea sandstone cores.
- Run special core analysis for the determination of relative permeability values at temperatures, 23°C, 0°C, -5°C, and -10°C.
- Determine of relative permeability values of both cores at salinities: 0 ppm, 6467 ppm and 5626 ppm.
- Conduct capillary pressure experiments to find the average pore radius of the sample.
- Conduct a theoretical analysis to determine the implications of freezing of interstitial water on relative permeability with change in salinity of water.
- Investigate the effects of interfacial tension (IFT), saturations, and pore geometry on relative permeability.
- Perform core flood experiments with fluids like deionized water, saline water, and antifreeze to propose the best production strategy.

Chapter 2 Background

2.1 Permafrost

Permafrost is a regular feature of extreme northern and southern terrain throughout the world, its boundaries dictated by the laws of physics. Defined as soil that has remained frozen (colder than 0°C or 32°F) for two or more years, permafrost, was first mentioned in the literature in Siberian military reports (Tsytovich, 1963). Permafrost can be found in soils and in rock sediments. Permafrost thicknesses range from less than 1 meter to greater than 1,000 meters. Regions underlain by permafrost occupy approximately 22.79 million square kilometers (about 24 percent of the exposed land surface) of the Northern Hemisphere (Zhang et al., 2003). Figure 5 shows the distribution of permafrost in the Northern Hemisphere.

Permafrost, discontinuous or continuous, prevails throughout most of Alaska. It ranges from a few inches in thickness at its southern margins, to 2,000 feet at Prudhoe Bay. There are many variations in what constitutes permafrost: it can contain over 30 percent ice or contain practically no ice at all. It can be overlain by several meters of snow, or by little or no snow. The incomplete freezing of water in dispersed soils and the dynamic equilibrium of unfrozen water and ice in frozen soils have been explained by investigations into the physics and mechanics of frozen soils.

Berea sandstone rocks were used in this study. These rocks certainly differ from soil characteristics. Though the above discussions are an important starting point for this study, the behavior of unfrozen water in frozen rock is probably different, because rocks are not as ductile as unconsolidated soils. However, the closest analog for the study of unfrozen water in a lithified rock residing in permafrost zone comes from studies of permafrost in soils.

Various techniques have been developed in order to quantify the unfrozen water content accurately and efficiently. Some of these techniques are helpful in finding the unfrozen water content in soils and rocks as well (Watanabe and Mizoguchi, 2002).

Frozen petroleum reservoirs contain oil, water, ice, and/or gas. This four-part composition makes a reservoir much more complex than a conventional reserve's three-part composition (oil, water, and/or gas).

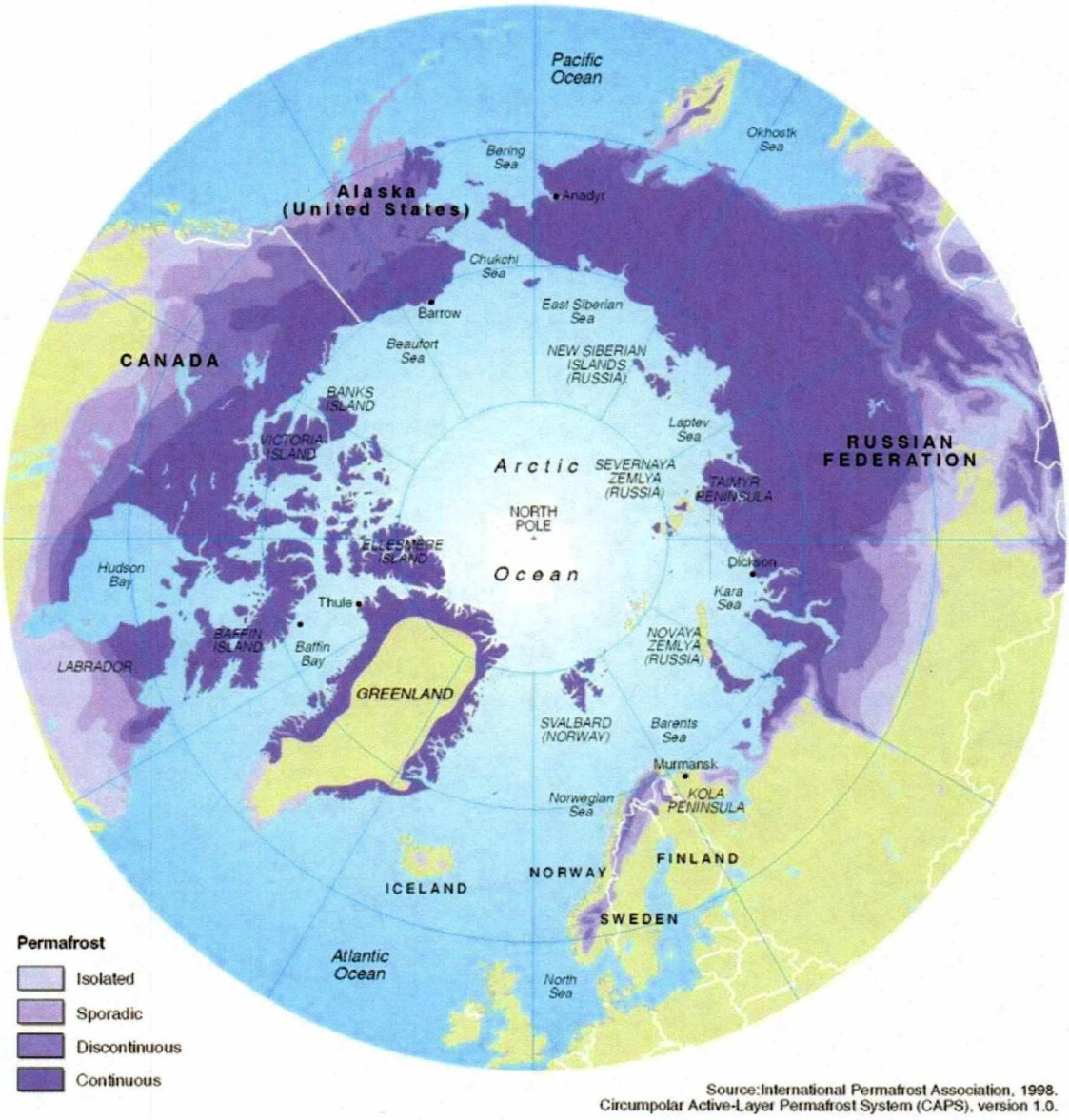

Figure 5: Distribution of permafrost in the Northern Hemisphere

(Permafrost distribution in the Arctic, 2005)

2.2 Unfrozen water

Liquid water layer can exist even at -30°C, where their thickness has been measured with pulsed NMR at an ice/silica interface in frozen porous silica (Ishizaki, 1995). Anderson and Tice (1971) showed that water can be in an unfrozen state until the ambient temperature reaches as low as -60°C to -35°C in a clay-water system. Unfrozen water can be found even at -125°C in coal (Mraw and Naas-O'Rourke, 1979). Therefore, at least some portion of the water associated with soil is expected to remain liquid in naturally occurring permafrost.

Unfrozen water's properties highly depend on temperature, pressure, water salinity, and mineralogy. Physicochemical properties of the soil, such as specific surface area, surface charge density, and the suite of exchangeable ions also influence water properties (Kleinberg and Griffin, 2005; Watanabe and Mizoguchi, 2002). The experimental results derived by Christ and Kim (2009) revealed that the amount of unfrozen water in silt decreased with decreasing temperature and stabilized at temperatures below -10°C (Watanabe et al., 2002). Also, when a porous medium is saturated with a solution, the amount of unfrozen water increased with increasing solute concentration (Watanabe et al., 2002). Pure water remains unfrozen in pores smaller than 0.004 μm in diameter even at below–zero temperatures. As the temperature increased, ice was shown to melt in successively larger pore spaces (Kleinberg and Griffin, 2005). The relationship between unfrozen water content (W_u) and temperature (T, °C) obtained through the pulsed NMR technique is shown in Figure 6. An Equation to calculate the unfrozen water content derived from results of NMR technique is given as

$$W_u = 19.8 * (T_m - T)^{-0.30} \quad (1)$$

Where,

T_m = Normal melting point, °C

W_u = Unfrozen water content

T = Temperature, °C

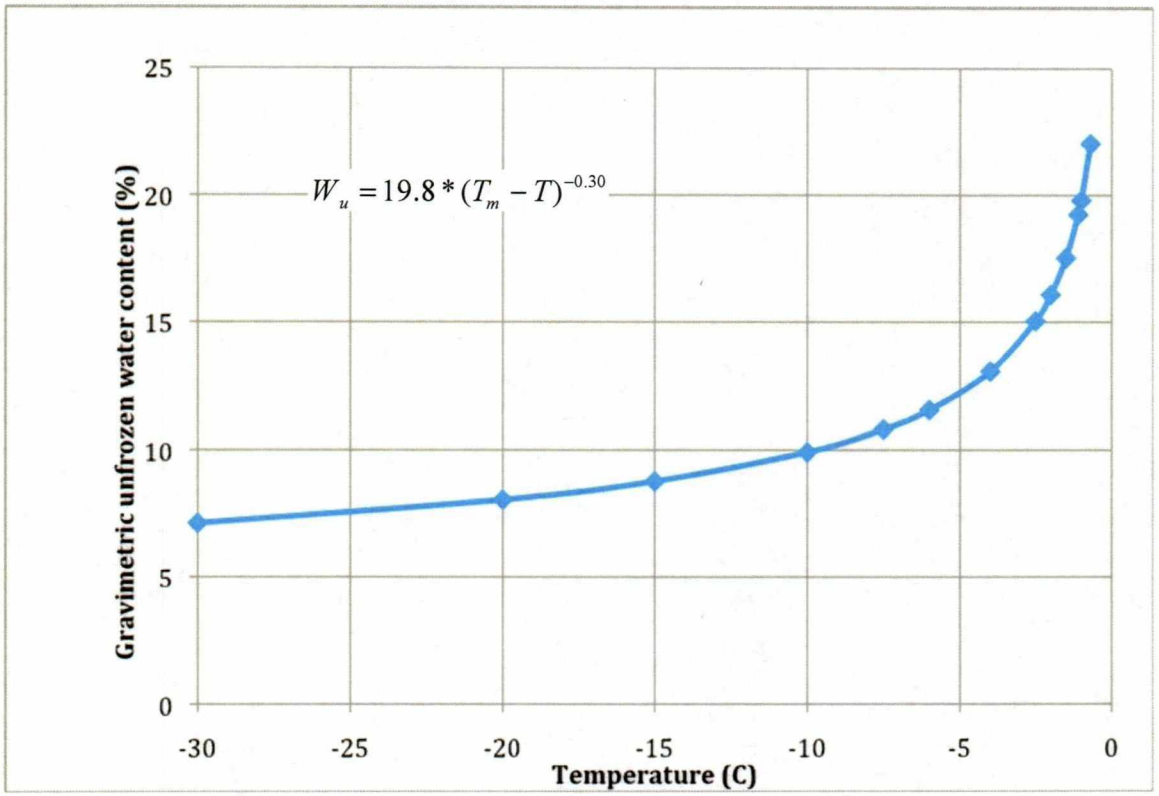

Figure 6: Relationship between unfrozen water and the temperature (Ishizaki et al., 1996)

The depression of the melting point by capillary forces is (Watanabe and Mizoguchi, 2002; Anderson et al., 2003)

$$\Delta T = -T_m \frac{2\gamma_{si}\cos\theta}{\rho_s \Delta H_m D} \tag{2}$$

Where

ΔT = Depression of the melting point, K,

T_m is the normal melting point, K,

γ_{sl} is the surface tension of the liquid water-ice interface, J/m^2,

θ is the contact angle between ice and the pore wall,

ΔH_m is the enthalpy of melting per unit mass, J/kg,

ρ_s is the density of the solid, kg/m^3, and

D is the diameter of the cylindrical capillary (Pore throat), μm,

Using literature values,

$T_m = 273.15$ K,

$\Delta H_m = 3.34 * 10^5$ J/kg,

$\rho_s = 916.2$ kg/m3.

The surface tension of the water–ice interface is $\gamma_{si} = 3.2 * 10^{-2}$ J/m^2 and $\Theta = 0°$,

$$\Delta T = -(0.057\ \mu m K)/D \tag{3}$$

2.3 Reasons for occurrence of unfrozen water in frozen ground

At temperatures below 0°C, the occurrence of unfrozen water in porous media such as soil or rock can be attributed to three main phenomena (Dash et al., 1995; Wilson et al., 1999).

1. Standard melting point depression: Solutes dilute the solvent and decrease its chemical potential.
2. Surface melting: Wetting the solid surfaces with a melted layer reduces the free energy.
3. Presence of curved surfaces: The amount of unfrozen water at sub-zero temperatures is determined by the sizes and shapes of the ice crystals, impurity concentrations, and microscopic soil structure (Reed et al., 1979).

2.4 Investigation of prevailing ice within the pore

In Section 2.2, the phenomenon of unfrozen water even below the freezing point of water in soil structures was explained. Section 2.3 detailed how unfrozen water might occur. Going forward, this investigation will analyze whether the grain surface surrounding the pore is in contact with this liquid water or with the frozen water (i.e., ice).

Kleinberg et al. (2004) performed an NMR experiment on two samples taken from a sandstone reservoir and a mud stone reservoir at below 0°C temperatures and

allowed to thaw to 18°C. His experiments showed that the unfrozen water was in contact with the grain surface, while the ice tended to reside in the interior of the pore space.

2.5 Reliance of water saturation on relative permeability and quantifying unfrozen water

Each phase's relative permeability depends on the phase's saturation of that phase. Water saturation (S_w, %) influences relative permeability.

$$S_w = \frac{V_w}{PV} * 100\% \quad (4)$$

Where,

S_w = Saturation of unfrozen water

V_w = Volume of unfrozen water in the pore space, ml or CC

PV = Total pore volume, CC

and the relative permeability (k_{rw}) can be measured as

$$k_{rw} = \frac{k(S_w)}{k} \quad (5)$$

Where,

$k(S_w)$ = permeability at water saturation S_w

k = permeability of fully liquid-water-saturated sediment.

The complexity of the structure and the chemistry involved theoretically render it impossible to predict the amount of liquid water (V_w) in frozen bulk soil (Dash et al., 1995). Because of this, experimental approaches to measure this variable as accurately as possible are needed.

In past studies, several methods have been implemented for quantifying the unfrozen water content in frozen soil. Some of these methods are:

1) Gravimetry
2) Neutron Thermalization
3) Gama Densitometry
4) Differential Scanning Calorimetry (DSC)

5) Conductivity
6) Time-Domain Reflectometry (TDR)
7) Nuclear Magnetic Resonance (NMR)

Each technique has their own distinct disadvantages that could lead to ambiguity in analyzing results. However, among these technique, NMR generally is considered the most accurate method for determining unfrozen water content of soils (Tice et al., 1982).

2.6 Behavior of unfrozen water content (θ) with changes in temperature (T)

A NMR spectroscope also can be used to study the relationship between temperature and liquid water content (θ) in frozen pores. Studies conducted by Ishizaki et al. (1996) and Watanabe and Mizoguchi (2002) revealed that the liquid water content in this relationship is nearly independent of temperature above 0°C. Below 0°C, it follows an exponentially increasing trend until the freezing point.

2.7 Frozen reservoirs

The Gubkin gas field (Russia) (Jensen et al., 1983), the northern part of the Timan- Pechora oil and gas field (Russia) (Jensen et al., 1983), and the Umiat oil field (U.S.) (Baptist, 1960) are examples of reservoirs that are found in permafrost (frozen ground). While the current study is generally applicable to any frozen reservoir, temperature and salinity of formation water values used in this study were taken with reference to Umiat reservoir. A discussion on the reservoir conditions, geology, and well placements of Umiat is necessary.

2.8 Umiat reservoir

Umiat reservoir resides in the permafrost zone. The Umiat oil field is located in the eastern part of the National Petroleum Reserve (NPRA), which is adjacent to the Colville River. Discovered in 1946, it is 92 miles from the Trans Alaska pipeline and about 220 miles south of the Prudhoe Bay oil field. The reservoir encompasses an area 37,000 square miles entirely overlain by continuous permafrost (as shown in Figure 7). The map in Figure 8 shows the geographic location of Umiat oil field. The reservoir at Umiat field is prototypical of a frozen reservoir: ice is one of its primary components. Some exploration has occurred at Umiat: the U.S. Navy and United States Geological Survey (USGS) have conducted research in this field, and there are 11 wells on the Umiat anticline (Gates and Caraway, 1960).

Table 1 summarizes permafrost depths in which the oil producing sands are located. The bottom part of the permafrost at Umiat ranges from 800 ft to 1,100 ft. Some part of the reservoir pay zone, which ranges from 275 ft to 1100 ft in depth, is thus in the permanently frozen zone. Reservoir pressure at Umiat ranges from 50 psi near the top to 350 psi near the bottom. Bubble point pressure is 328 psi. The initial pressure support for the reservoir, supplied by solution gas drive, was able to produce for only three months. The shallowness of the reservoir results in poor initial pressure support (Baptist, 1960). The oil at Umiat is light (36–37.2 degree API) and it is sweet, containing a sulfur content of less than 0.1 percent (Potter and Moore, 2003). However, remoteness of the field, frozen conditions of the reservoir, and poor pressure support (lack of aquifer support) make exploration of and production from Umiat a real challenge.

Johnson (2010) estimated original oil in place as 1.9 billion barrels. According to Baptist (1960), estimations of economically recoverable oil range from 30 million bbl to over 100 million bbl, with an average estimate of 70 million barrels. Renaissance Alaska Inc's estimation of proved, probable, and possible recoverable reserves is 250 million barrels of oil (Watt et al., 2010).

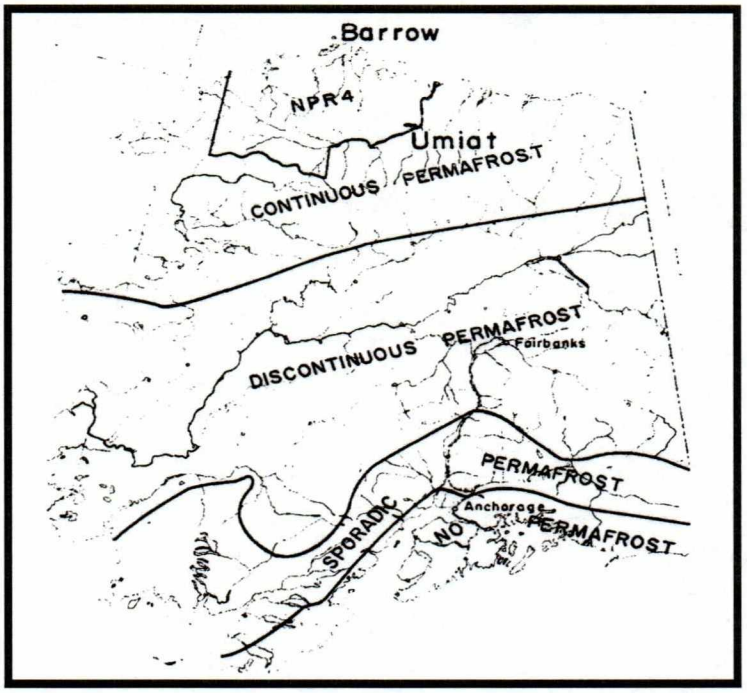

Figure 7: Permafrost zones and Umiat field (Gates and Caraway, 1960)

Table 1: Data of permafrost in different wells at Umiat (Baptist, 1960)

Well Number	**1**	**4**	**5**	**6**	**7**	**9**	**11**
Surface elevation (ft)	810	483	335	337	300	424	481
Depth to top of lower sand (ft)	1,818	745	770	1,055	1,200	866	2,805
Elevation of top of lower sand, below sea level (ft)	1,800	262	435	718	870	442	2,324
Depth to base of permafrost (ft)	920	890	800	770	827	1,055	770
Elevation of base of permafrost below sea level (ft)	110	407	465	433	497	631	289
Liquid production from lower sand	water	oil	oil	water	water	oil	water

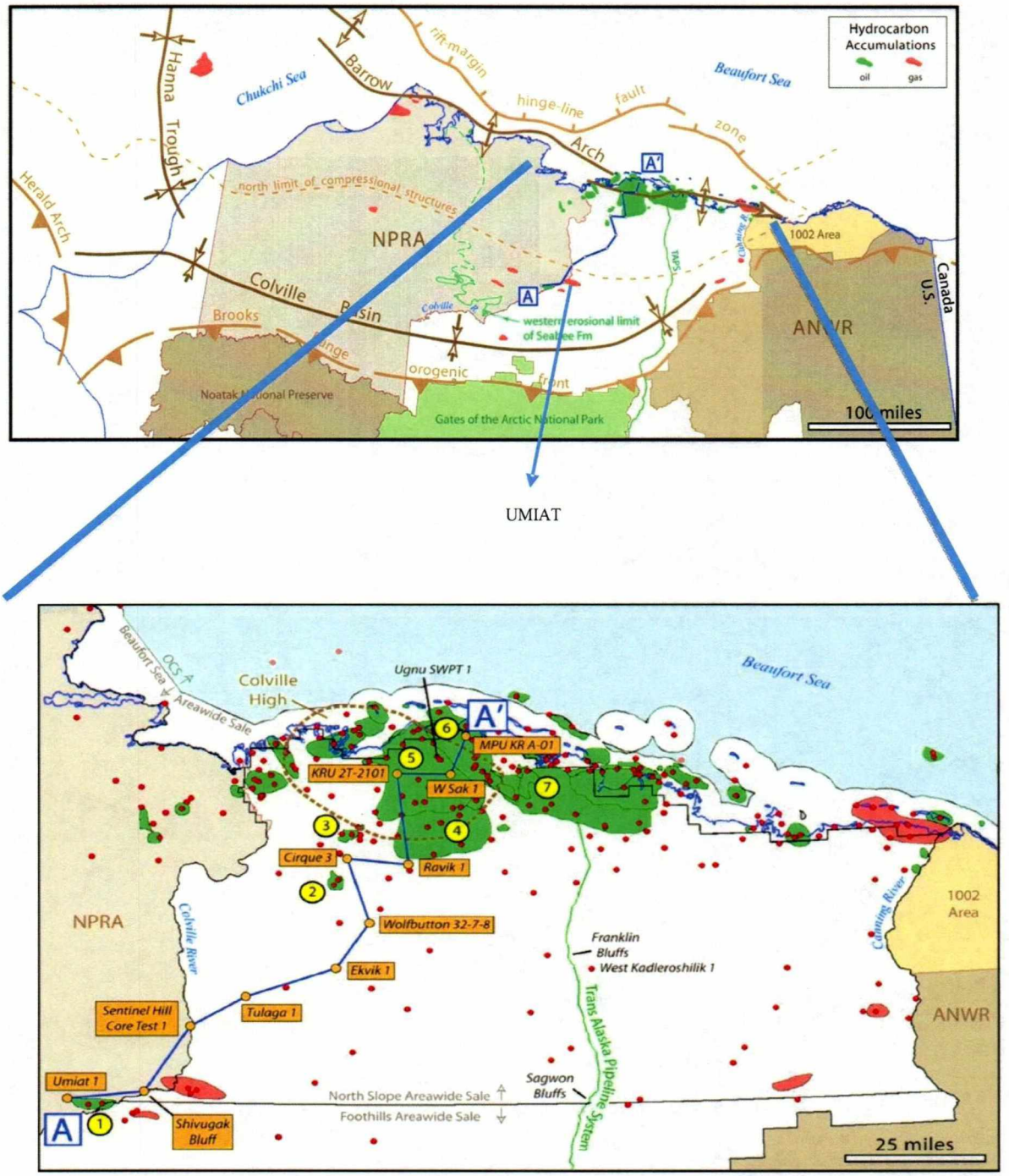

Figure 8: Geographic location of Umiat oil field. (1) Umiat, (2) Meltwater, (3) Tarn, (4) West Sak, (5) Kuparuk River, (6) Milne Point, and (7) Prudhoe Bay (Decker, 2007)

2.8.1 Geology

Umiat field consists of Cretaceous sandstones deformed into an anticline (Collins, 1958). The Umiat reservoir consists of Torok–Nanushuk and Seabee–Tuluvik Formations (Figure 9.A). The Nanushuk consists of deltaic, fluvial, and estuarine facies (LePain et al., 2009). The informal formations of Umiat are listed below (from top down) (Figure 9.B) (Shimer, personal communication 2009)

- Ninuluk formation: Dominated by shallow marine sandstone and mudstone
- Chandler formation: Dominated by delta plain mudstone and channel sandstone
- Upper Grandstand: Consists of 50-75 ft of deltaic sandstone.
- Shale barrier: Consists of 350 ft marine to marginal marine mudstone
- Lower Grandstand: Up to 200 ft of shallow marine sandstone
- Marine shale: Underneath Nanushuk and Torok formation

Oil that could be recovered economically from Umiat reservoir is found in the Upper Grandstand and Lower Grandstand formations (Collins, 1958)

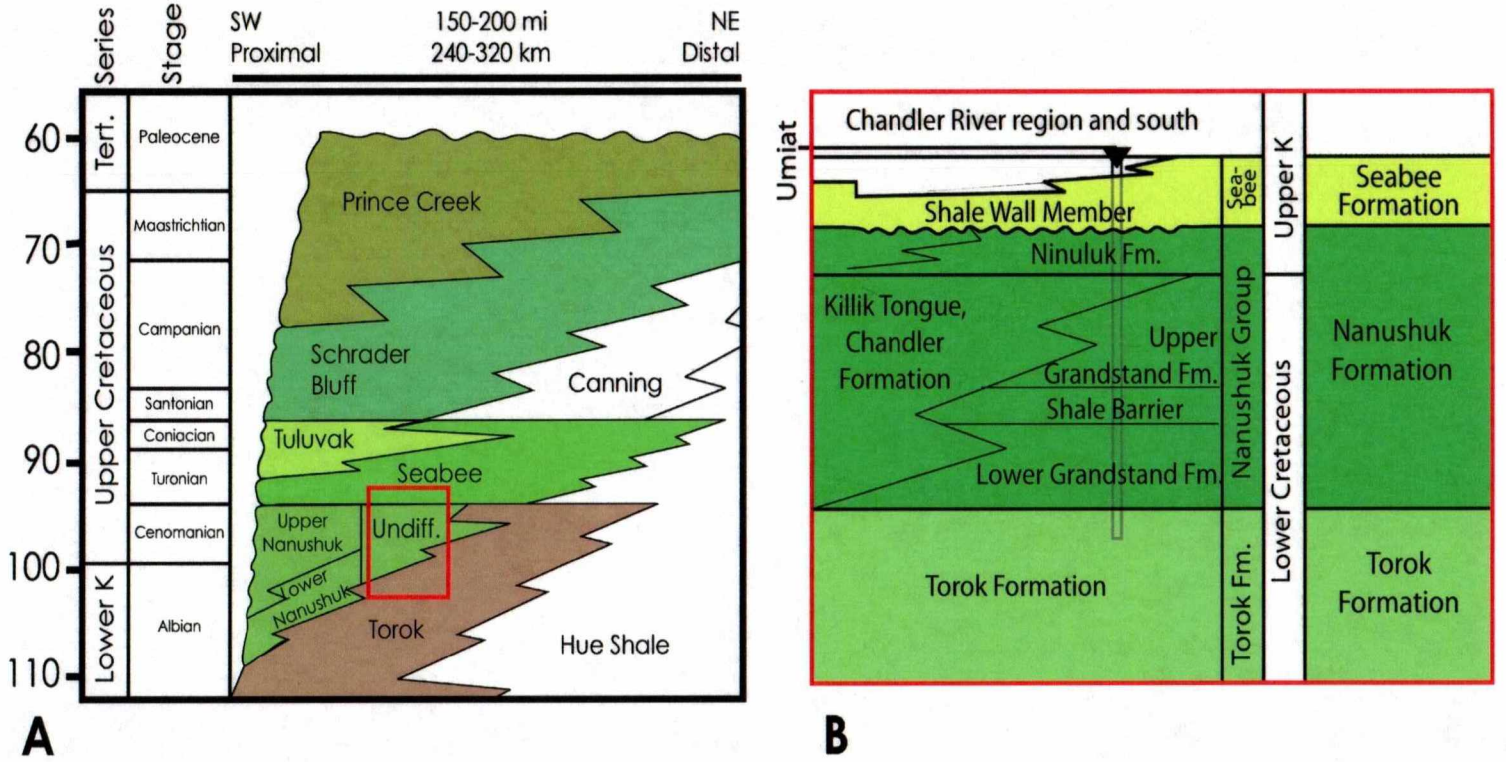

Figure 9: A) Relevant Brookian stratigraphic units in the Umiat area include the Torok, Nanushuk, Seabee, and Tuluvak formations (modified from Mull et al., 2003 by Shimer (personal communication, 2011)). B) The informal nomenclature for the Nanushuk Formation in the Umiat area is useful for the interpretation of significant sequence stratigraphic surfaces and systems tracts (modified from Mull et al., 2003 by Shimer (personal communication, 2011)).

2.8.2 Drilling and completion

The Umiat anticline, 10 miles long by 3 miles wide, contains a total of 11 test wells drilled for exploration purposes (Gates and Caraway, 1960). Of these 11 wells, only 6 have returned considerable amounts of oil. Figure 10 shows the location of the 11 wells at Umiat.

Wells 1, 2, and 3 were drilled with water-based mud using conventional rotary methods. Wells 1 and 2 were failures, producing nothing (Gates and Caraway, 1960). Well 3 produced an average of 24 b/d. Later on, wells 4, 6, 8, and 10 were drilled using cable tools and brine. An average of 70 b/d of production was achieved among the four wells. Initially, well 5 was drilled using brine. It was then widened using rotary tools and oil–based mud. Post-widening, an average production rate of 400 b/d was recorded at well 5. Well 9, drilled using oil-based mud, returned an average production of 300 b/d. Figure 11 shows the production capacity of Umiat wells, while accounting for the drilling method (Gates and Caraway, 1960).

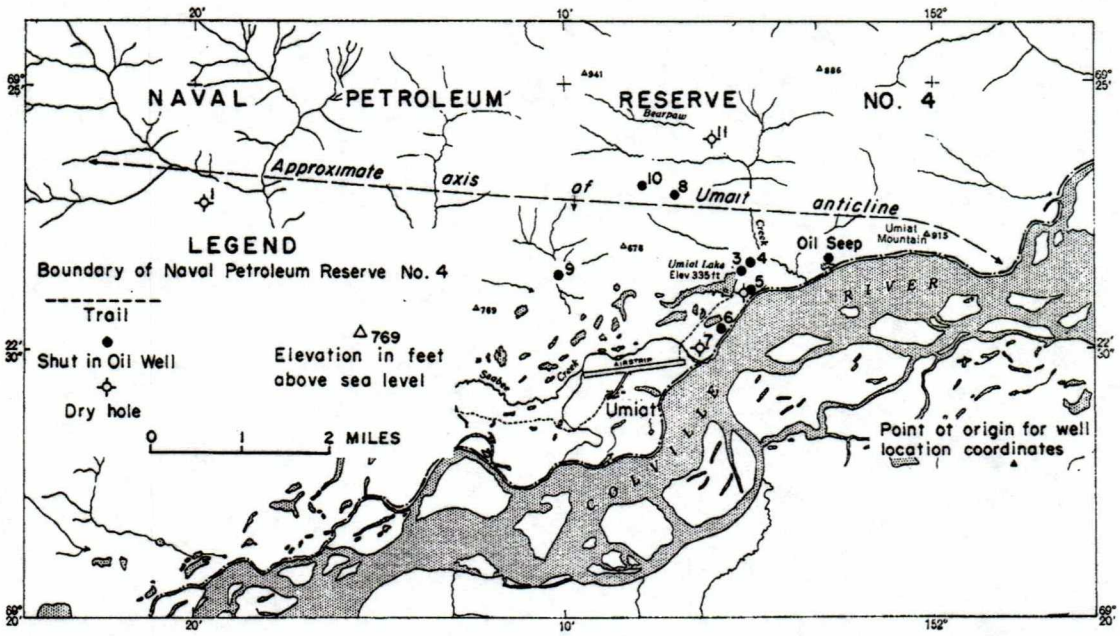

Figure 10: Well location at Umiat field (Gates and Caraway, 1960)

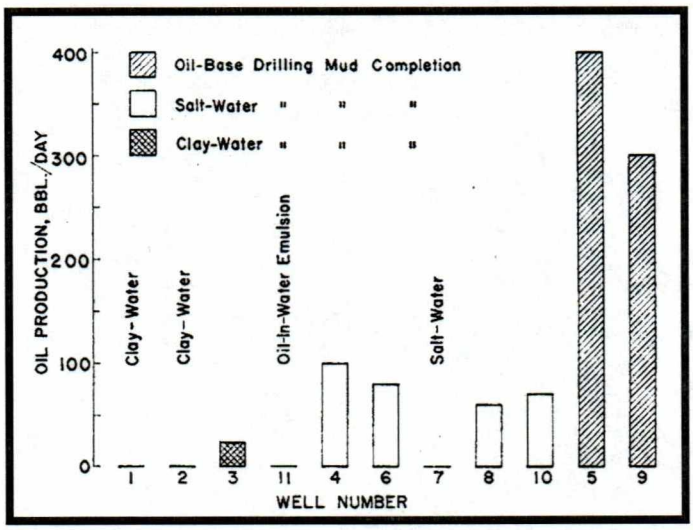

Figure 11: Production capacities of wells related to drilling mud (Gates and Caraway, 1960)

2.8.3 Depth of the permafrost

Placing thermistor cables in the wells and measuring the geothermal gradient determined the depth of the permafrost at Umiat (Gates and Caraway, 1960). The geothermal profile in well 6 is shown in Figure 12.

In well 9, between the depths of 100 and 870 ft the temperature increases at a rate of 1.33°F/100 ft in well 9. The geothermal gradient in wells 6 and 8 is 1.56°F/100 ft. The temperature-depth profile in well 9 indicates that the depth of the permafrost is 1055 ft, which is almost 150 feet deeper than permafrost depth found at any other Umiat well. Depths to the base of the permafrost for all Umiat wells in which temperature gradients were measured are shown in Table 1.

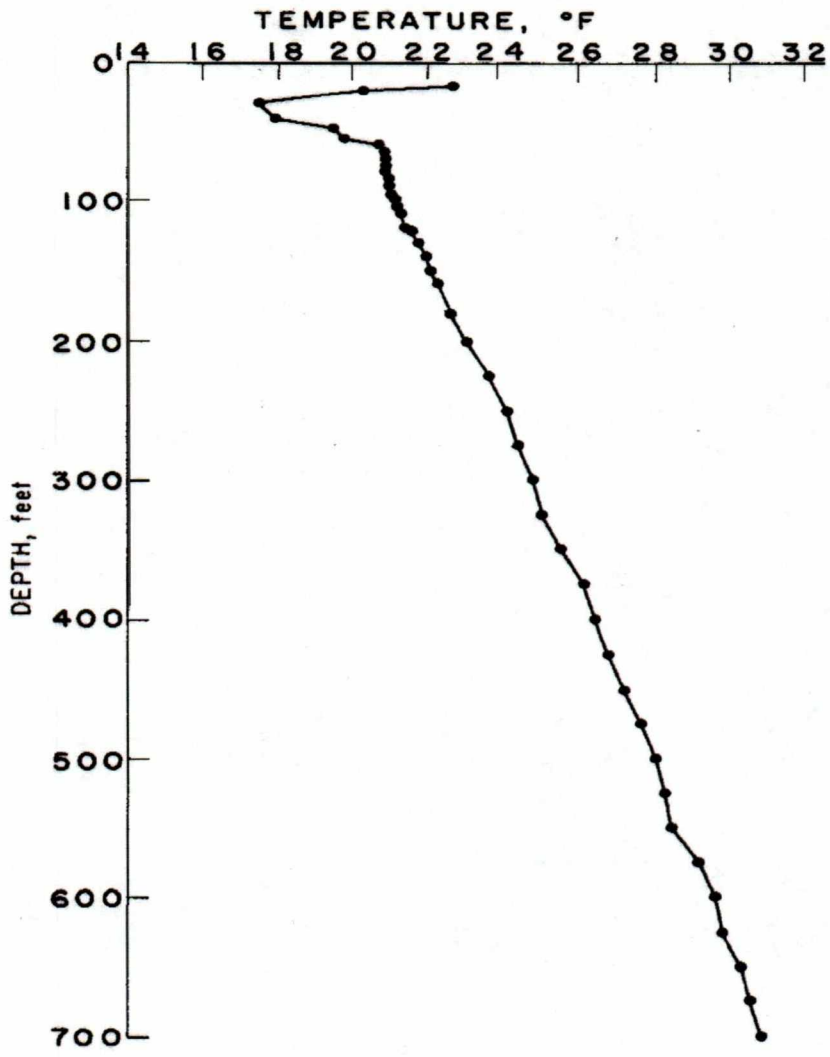

Figure 12: Temperature – depth profile of well 06 (Gates and Caraway, 1960)

2.9 Relative permeability

Absolute permeability is a measure of the ability of a rock to transmit a single fluid phase through its pore structure (Dandekar, 2006). Permeability is measured in Darcy or millidarcy (md) and is determined by the size of the pore throats, the connecting

passage between pores. Permeability often decreases with depth because compaction and cementation restricts or blocks the pore throats, in effect reducing the flow rate.

Darcy performed an experiment of the flow of fluid (water) through a bed of sand (Freeze, 1994). This experiment is similar to the diagram of flow of fluids through a core plug shown in Figure 13.

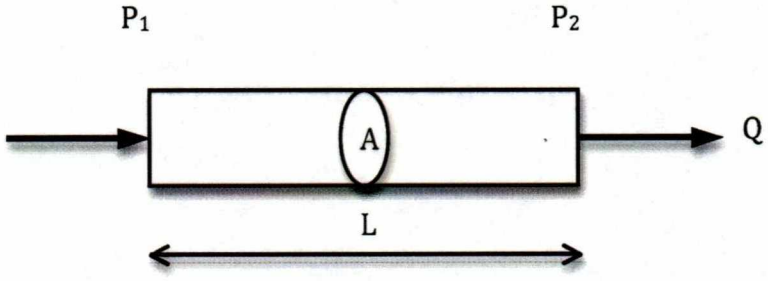

Figure 13: Schematic of fluid flow through core plug (Dandekar, 2006)

Absolute permeability of the sample can be calculated using Darcy's law. Darcy's law is given as

$$Q = \frac{kA\Delta P}{\mu L} \tag{6}$$

Where,

Q = Volumetric flow rate through core plug, CC/sec

k = Absolute permeability, Darcy

A = Area of cross section of core plug, sq. cm

$\Delta P = P_1 - P_2$ = Pressure differential across the core plug, atm

μ = Viscosity of the fluid, cp

L = Length of the core sample, cm

Darcy's experiments were restricted to sand bodies 100% saturated with water. However, later investigations suggested that Equation 6 could also be used for other fluids with corresponding 'μ' value (Dandekar, 2006).

The measure of relative permeability is the ratio of effective permeability of a particular fluid at a particular saturation to the absolute permeability of that fluid at total saturation. The effective permeability is a measure of flow of one phase when the

medium is saturated with multiple phases. If a single fluid is present in a rock, its relative permeability is 1.0. Relative permeability allows comparison of the different abilities of fluids to flow in the presence of each other, because the presence of more than one fluid generally inhibits flow.

2.10 Determination of relative permeability

The following two sections discuss the most common flow experiments for determining relative permeabilities:

1. Steady-State (SS)
2. Unsteady-State (USS).

2.10.1 Steady-State technique

The steady-state method was first developed in 1939 by Leverett. Each step of the procedure involves the simultaneous injection of two phases, at a certain volumetric ratio, into the core plug. The injection continues until the pressure drop across the core plug is stabilized and the influent and effluent volumetric ratios are equal. This condition is called a Steady-State condition. Once this condition is reached, the core must be removed from the core holder. Then, using the mass-balance equation, the fluid saturations are found. At these saturations we can find the effective permeability of each fluid using Darcy's law. Dividing the effective permeabilities by absolute permeability or by the effective permeability to oil at irreducible water saturation, we get the relative permeabilities. In subsequent steps, the volumetric ratio of injected fluids is progressively increased. When the steady-state condition is reached, the new saturations of fluids and their relative permeabilities can be found.

Calculation of relative permeabilities using the steady-state method is simple, but from a practical point of view, the experiment is time consuming. This is because at each step we need to wait until the steady-state condition is achieved. Also, at each step we

need to remove the core from the core holder. This procedure might result in fluid loss, especially if we are measuring gas-oil relative permeabilities (Dandekar, 2006).

2.10.2 Unsteady-State technique

In terms of the laboratory experiments, unsteady-state technique is easier than steady–state technique, but it requires much more data processing. Unsteady–state technique was used in this work. Core flooding experiments can be carried out in order to determine relative permeability. In this procedure, the core sample is flooded with oil/water, depending on the saturated phase of that sample. The core is placed in a freezing chamber or cooling jacket surrounding to maintain a constant test temperature (Godabrelidze, 2010). The common method for analyzing these data is the Johnson-Bossler-Naumann (JBN) method (Johnson et al., 1959).

An alternate method involves the following technique also could be applied.

$$k_{ro} = \frac{k_{eo}}{k} \quad and \quad k_{rw} = \frac{k_{ew}}{k} \tag{7}$$

Where

$$k_{eo} = \frac{q_o \mu_o L}{A \Delta P} \; at \; S_w \tag{8}$$

$$k_{ew} = \frac{q_w \mu_w L}{A \Delta P} \; at \; S_w \tag{9}$$

$$S_w = \left(1 - \frac{Cumulative\ volume\ oil\ produced}{Pore\ volume\ of\ the\ sample}\right) * 100\% \tag{10}$$

Where

k_{eo} , k_{ew} = Effective permeability of oil and water respectively.

q_0, q_w are volumetric flow rates of oil and water respectively from experiment, CC/sec

S_w = Water saturation, %

μ_0, μ_w = Viscosity of oil and water respectively, cp

A = Cross–sectional area of core sample, sq. cm

L = Length of the core plug, cm

ΔP = Pressure differential across core plug, atm/sec

This alternative method was used in this study to determine the effective permeabilities.

2.11 Reduction in relative permeability to oil and oil recovery

Baptist (1960) performed core flood experiments on six Umiat core samples. His purpose was to determine the relative permeability to oil and oil recovery through solution gas drive. An increase in oil recovery was observed at 75°F (24°C), relative to recovery at 26°F (-3°C). As shown in Table 2, average recovery of oil at 75°F was 40%, while recovery at 26°F was just 29%.

The relative permeability of the six Umiat core samples was also determined by Baptist (1960) at a room temperature of 70°F (21°C) and below the freezing point of water at 26°F. A reduction of 23.3% in relative permeability was observed for Sample 1 from 70°F to 26°F. A reduction of 31.5% was observed on the relative permeability of Sample 2 from room temperature to below zero.

Baptist explained that the freezing of interstitial water was a reason for the reductions in relative permeability and oil recovery. This was also the reason for the increase in irreducible water saturation from 41% to 44%. Apart from freezing of interstitial water, there is a possibility of other factors causing this for reduction in relative permeability to oil, such as fluid saturations, pore geometry and interfacial tension effects between the different phases of the reservoir. This study concentrates on the reasons behind the reduction in relative permeability to oil in frozen reservoir.

Table 2: Oil recovery experiments on Umiat core sample at 23°C and -3°C (Baptist, 1960)

Well and sand	Depth, feet	Porosity, %	Air permeability, md	Initial oil saturation, %PV		Solution-gas expansion				Gas drive			
						Recovery initial oil, percent		Residual oil, percent pore volume		Recovery initial oil, percent		Residual oil, percent pore volume	
				Brine	oil	26^0F	75^0F	26^0F	75^0F	26^0F	75^0F	26^0F	75^0F
Umiat # 2, lower	796	16.4	196	37	63	34	48	42	33	21	20	28	20
	797	15.1	49	44	56	27	29	41	39	7	9	36	34
	805	14.6	92	41	59	17	-	49	-	28	-	33	-
Umiat #3, upper	259	18.2	128	42	58	36	-	38	-	34	-	19	-
	352	17.7	134	38	62	31	50	43	34	26	23	27	16
	355	16.3	52	44	56	25	33	42	38	19	34	32	19

2.12 Possible reasons for reduction in relative permeability

Key parameters that affect relative permeability include (Dandekar, 2006):

1) The pore-space geometry (the distribution of large and small conduits and their sizes)
2) Viscosity of the fluid
3) Wettability of the mineral surface, and
4) Interfacial tension (IFT) (and/or surface tension) between the fluid phases and between each fluid phase and the minerals.

These parameters are the major factors in a 3-component system (oil-water-gas). In a four-component system (oil-water-gas-ice), along with the above parameters, the freezing of water within porous media also has a significant effect in altering the relative permeability of each phase.

Interfacial tension (IFT) between different fluids of the system also alters the relative permeability to oil. Shen et al. (2005) performed experiments with different values of IFT and proposed several empirical equations of relative permeability as a function of IFT. In the case of frozen reservoirs, additional interfacial tension values exist between ice and other fluids of the reservoir. The net interfacial tension is the summation of all interfacial tensions that exist between the fluids of the formation (Konno and Izumiyama, 2002).

2.13 Kozeny–Carman equation

Kozeny (1927) proposed an equation largely used in fluid dynamics that was later modified by Carman (1937). The resulting equation, Kozeny–Carman equation or KC equation, is expressed, similarly to Darcy's law, as "Flow of fluid is directly proportional to pressure drop and is inversely proportional to viscosity." The KC equation was developed after consideration of the flow of fluid through a packed bed of solids (Chapuis and Aburtin, 2003). The KC equation is given as

$$\frac{\Delta P}{L} = \frac{150\overline{V_0}\mu}{\phi_s^2 D_P^2}\frac{(1-\varepsilon)^2}{\varepsilon^3} \tag{11}$$

Where,

ΔP = Pressure drop, atm

L = Length of the packed bed, m

Φ_s = Spericity of the grain particles

ε = Porosity, %

D_p = Diameter of the particles, m

V_0 = Superficial velocity, m/sec

This KC equation is valid for single-phase laminar flow. Since the equation was established, it has taking several forms. Governed by several assumptions, alternative form of this equation is used in this study to find the radius of ice formed in the center of the pore. Assumptions and the alternative form of the equation are discussed in detai in Chapter 4.

2.14 Berea sandstone

Berea sandstone is used as a model rock to perform experiments for relative permeability and production techniques. It has a porosity of 20% and an air permeability of 180md. These are homogeneous cores with good permeability values, and are standard cores that have been widely used in the literature for core flooding experiments. Therefore, for the present work, Berea sandstone was chosen for the core flood experiments. Berea sandstone was ordered according to the required length and diameter (6" X 1.4"). It was placed under permafrost conditions to measure the relative permeability to oil in the presence of ice, and the results and analysis can be compared to the results derived from any frozen cores.

Chapter 3 Experimental procedure

In order to determine the sensitivity of relative permeability to oil with temperature and salinity, core flooding experiments were performed on two clean Berea sandstone cores. Core flooding experiments consist of two types of core analysis: routine and special core analysis. Routine core analysis helps in finding porosity, permeability, and saturations. Special core analysis contributes in determining relative permeability. Berea sandstone rocks were subjected to permafrost conditions for this experimental study. The cores used are cylindrically shaped, 6 inches in length (L) and 1.4 inches in diameter (d) (Figure 14). They are designated Core 1 and Core 2. Both cores were cleaned and dried after one set of experiments. However, Figure 14 shows difference between cleaned (Core 1) and used (Core 2) cores.. Air-permeability tests were made on these samples using a probe permeameter. Vertical air permeability of Core 1 and Core 2 were respectively 187 md and 180 md.

The experimental setups used for routine and special core analysis and test procedures are explained in the following sections. Even though the present work is a generalized study for all frozen reservoirs, the reservoir conditions, including temperature and pressure of the Umiat reserve were used to perform these experiments.

Figure 14: Berea sandstone cores labeled Core 1 and Core 2.

3.1 Experimental setup

Godabrelidze (2010) built the experimental setup and developed the test procedure for the core flood experiments. The setup shown in Figure 15 consists of a core holder, hydraulic pump, positive displacement pump, accumulators, pressure gauges, and cooling chamber.

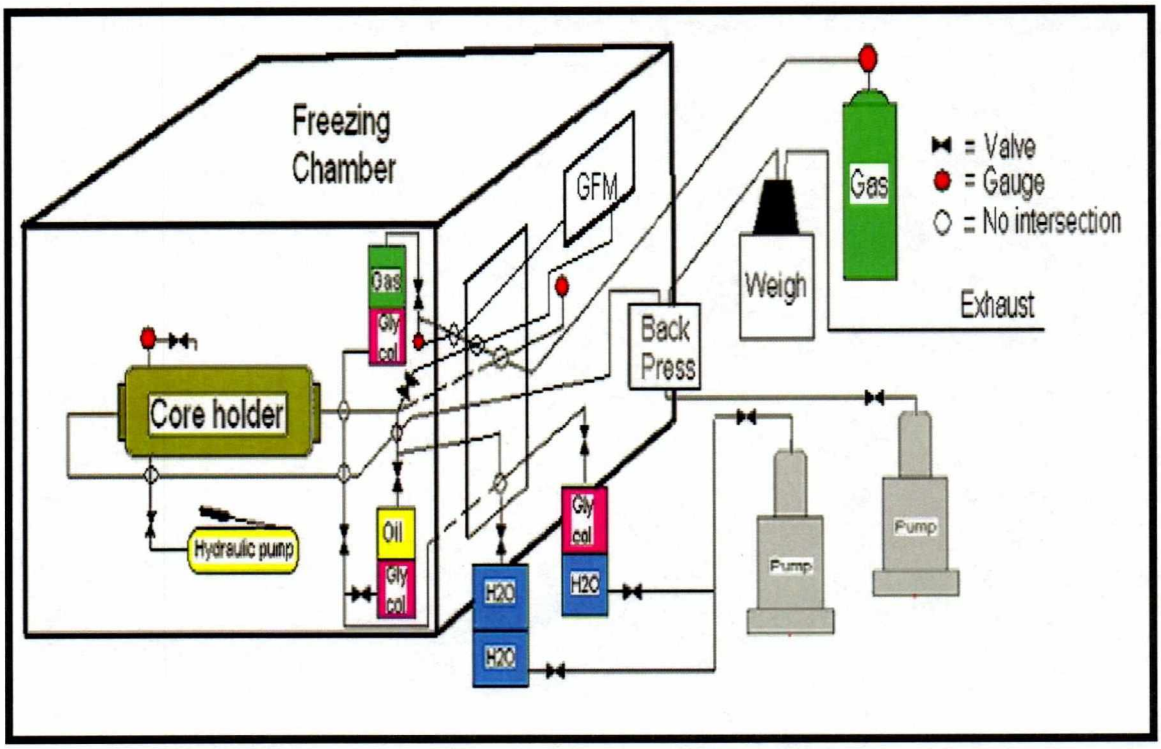

Figure 15: Experimental setup of core flood experiments (Godabrelidze, 2010)

To perform the flooding experiments, the core is placed in the core holder. Initially the core is mounted on a rubber sleeve and then placed in the core holder. The ductility of this rubber sleeve helps maintain an overburden pressure. Overburden pressure is transferred to the core by a hydraulic pump in order to simulate reservoir pressure. The core holder has inlet and outlet openings for the fluid to pass through the core.

In the process of creating overburden pressure, the hydraulic pump displaces the hydraulic oil (kerosene in this case) into the annular space between the rubber sleeve and the metal jacket of the core holder.

A positive displacement pump is used to inject flooding fluids into the core. The pump is filled with water and displaces other fluids (such as water, antifreeze or oil) stored in the accumulators by pushing the piston upwards. After some trial and error, a flow rate of 0.05 cc/sec was found to be most effective, causing only minimum effects of turbulence due to frictional force.

Three accumulators having water, oil, and antifreeze, respectively, were used in this experiment (Figure 15). The inlet of the accumulator is connected to the outlet of the positive displacement pump. Careful operation of valves allows only the desired fluid to enter into the core holder for flooding.

To measure the pressure differential across the core, a pressure transducer is connected to the inlet tubing. This pressure transducer converts pressure into an analog electric signal, which gives an accurate pressure reading up to two decimal points. To measure the overburden pressure that is applied on the core sample, another pressure gauge is located between the hydraulic pump and the core holder.

The system, consisting of a core holder, oil accumulator, and hydraulic pump, were situated in a cooling chamber to maintain the reservoir temperature conditions.

3.2 Experimental procedure

The experiments were carried out on both cores using a similar procedure. Routine core analysis helps find porosity and absolute permeability of the core. Special core analysis helps determine the effective permeability of oil.

3.2.1 Routine core analysis

Determinations of porosity, absolute permeability, and irreducible water saturation are required to advance the investigation. Routine core analysis is carried out at room temperature (23°C). The steps illustrated below are for Core 1.

Step 1: The dry weight (DW) of the core was measured before being subjected to saturation with deionized water. The core was then placed in a beaker of deionized water (0 ppm salts) and kept under a vacuum for 2 to 3 days. Water saturated the core by replacing the air in the pores. The core was removed from the beaker after it was 100% saturated with water. The wet weight (WW) of the core sample was measured and the sample was placed immediately in the core holder

Step 2: Meanwhile, density (ρ) and viscosity (μ) of the kerosene were measured at 23°C, 0°C, -5°C, and -10°C using an Anton–Paar density meter and a Brookfield viscometer (the test procedure for viscometer is explained in Section 3.3).

Step 3: Since the length (L, inches) and the diameter (d, inches) of the core are known, the bulk volume (BV) can be calculated as

$$BV = A * L \tag{12}$$

Where,

A = Cross sectional area of the core sample = $\pi \frac{d^2}{4}$

Step 4: The pore volume (PV) and porosity (ϕ) were measured as

$$PV = \frac{WW - DW}{\rho_w} \tag{13};$$

ρ_w = Density of corresponding water sample, lb/ft^3

Dry weight and wet weight of the core were measured in lbs.

Obtained PV is converted into cubic inches using a conversion factor of 1728 in^3/ft^3

$$\phi = \frac{PV}{BV} * 100\% \tag{14}$$

Step 5: After placing the core into the core holder, an overburden pressure of 600 psi was applied. The core was then flooded with the water sample at a constant flow rate (q) of 0.05 cc/sec until the pressure differential (ΔP) across the core stabilized. Since all inputs were specified, the absolute permeability of the core sample could be calculated using Darcy's law (Equation 6).

Step 6: After the pressure stabilized, the core sample was flooded with oil (kerosene) at the same flow rate until the pressure again stabilized. There also must be no more water production at the outlet. The amount of water remaining in the sample is immobile, and the corresponding saturation is called the irreducible water saturation (S_{wi}). By measuring the amount of water (Q_{wp}) collected at the other end, this water saturation can be calculated using the Equation

$$S_{wi} = \frac{PV - Q_{wp}}{PV} * 100\% \tag{15}$$

Step 7: The same procedure from Step 1 to Step 6 was repeated for Core 2.

3.2.2 Special core analysis

The relative permeability of the core samples to oil (k_{ro}) was calculated at four different temperatures and three different formation water salinities. The temperatures chosen were 23°C, 0°C, -5°C and -10°C. The relative permeability data were generated for both cores at all four temperatures. Relative permeability to oil (k_{ro}) data at room temperature (23°C) serves as a reference point for comparison of results of the other temperatures.

The formation water salinity could also potentially affect relative permeability. The effective permeability to oil at three different salinities was measured to help further understanding of the dependency of relative permeability of oil on the salinity of formation water. The three salinities used in the special core analyses were 0 ppm (deionized water), 6467 ppm (Salinity 1) and 5626 ppm (Salinity 2). Salinities 1 and 2 were chosen based on the salt composition of Umiat formation water (Godabrelidze, 2010). Deionized water was used as the reference salinity. The steps explained below were followed at 23°C and with 0 ppm water. A similar procedure is applicable for all temperatures and salinities of this experiment.

Step 8: Following Step 6 (Section 3.2.1), the effective permeability of oil (K_{eo}) @ S_{wi} was calculated using Equation 8. Since water is at its irreducible saturation, the effective permeability of water K_{ew} is zero.

Step 9: The relative permeability to oil (k_{ro}) was calculated using Equation 7 and is given as $k_{ro} = (k_{eo}/k)$

Step 10: The core was flooded with kerosene at a temperature of 0°C until the pressure stabilized.

Step 11: Step 8 and 9 were repeated to determine effective permeability of oil ($k_{eo}@S_{wi}$(ice)) and relative permeability to oil at 0°C.

Step 12: steps 8 to 10 were repeated with two more temperatures (-5°C and -10°C) at the same salinity.

Step 13: At the completion of the above set of experiments, the core was removed from the core holder, and then cleaned with toluene and acetone, and dried in the oven at 27°C for 2 days.

Step 14: After drying the core, Steps 1 to 13 were repeated with two more saltwater samples of concentrations 6,467 ppm and 5,626 ppm. Composition of the water used is shown in Table 3.

Table 3: Amount of salts in the water sample (Collins, 1958)

Used salts	**Salinity 1*** **g/6L**	**Salinity 2**** **g/6L**
Calcium Chloride ($CaCl_2$)	0.11	0.09
Sodium Sulfate (Na_2So_4)	0.25	0.13
Sodium Bicarbonate ($NaHCO_3$)	25.78	21.63
Sodium Chloride (NaCl)	8.4	4.91
Magnesium Chloride ($MgCl_2$)	0.07	0.11
Calcium Carbonate ($CaCO_3$)	0.02	.02
Sodium Carbonate (Na_2CO_3)	4.11	6.83
Magnesium Carbonate ($MgCO_3$)	0.003	.003
Barium Carbonate ($BaCO_3$)	0.009	.009
Total Salinity	38.75 g/6L or 6467 ppm	33.73 g/6L or 5626 ppm

* Salinity 1 was taken from Collins (1958).

** Salinity 2 was prepared by the author of this study.

3.2.3 Uncertainty of experimental data

Uncertainty in the calculations of effective permeability values by special core analysis for Equation 6 can be obtained by the standard approach explained by Coleman et al. (2009). The parameters used in Equation 6 are volumetric flow rates of fluid from the pump, the viscosity of the fluid (measured by Brookfield viscometer), the length and area of the core sample, and the stabilized pressure differential. The uncertainty in calculating relative permeability is produced with the calculation:

$$\frac{\delta k_{eo}}{k_{eo}} = \left[\left(\frac{\delta q_0}{q_o} \right)^2 + \left(\frac{\delta \mu_o}{\mu_o} \right)^2 + \left(\frac{\delta L}{L} \right)^2 + \left(\frac{\delta A}{A} \right)^2 + \left(\frac{\delta \Delta P}{\Delta P} \right)^2 \right]^{1/2} \tag{50}$$

For the ISCO pump, the uncertainty in measuring volumetric flow rate ($\delta q_o/q_o$) is 0.5%; for the Brookfield viscometer, $\delta \mu_o/\mu_o$ is about 1%; the uncertainty in length ($\delta L/L$) is 0.66%; and the uncertainty in pressure stabilization ($\delta \Delta P/\Delta P$) is 0.25%. Uncertainty in area is calculated as

$$\frac{\delta A}{A} = \left[2 \left(\frac{\delta d}{d} \right)^2 \right]^{1/2} \tag{51}$$

The uncertainty in diameter ($\delta d/d$) is about 2.81%. Using this number, the uncertainty in area ($\delta A/A$) was calculated as 3.97%. Finally, combining all the uncertainties together in Equation 50, the uncertainty in measuring the effective permeability of oil is ($\delta k_{eo}/k_{eo}$) ±4.2%. Similarly, the uncertainty in calculating the relative permeability to oil ($\delta k_{ro}/k_{ro}$) is ±5.94%.

The weighing balance has an error of 1%, which is the only uncertainty in finding connate water saturations.

3.3 Brookfield viscometer test procedure

Viscosity measurements were performed using a Brookfield viscometer. Viscosity is a measure of a fluid's resistance to flow. Figure 16 shows the experimental setup for finding the viscosity of a given fluid.

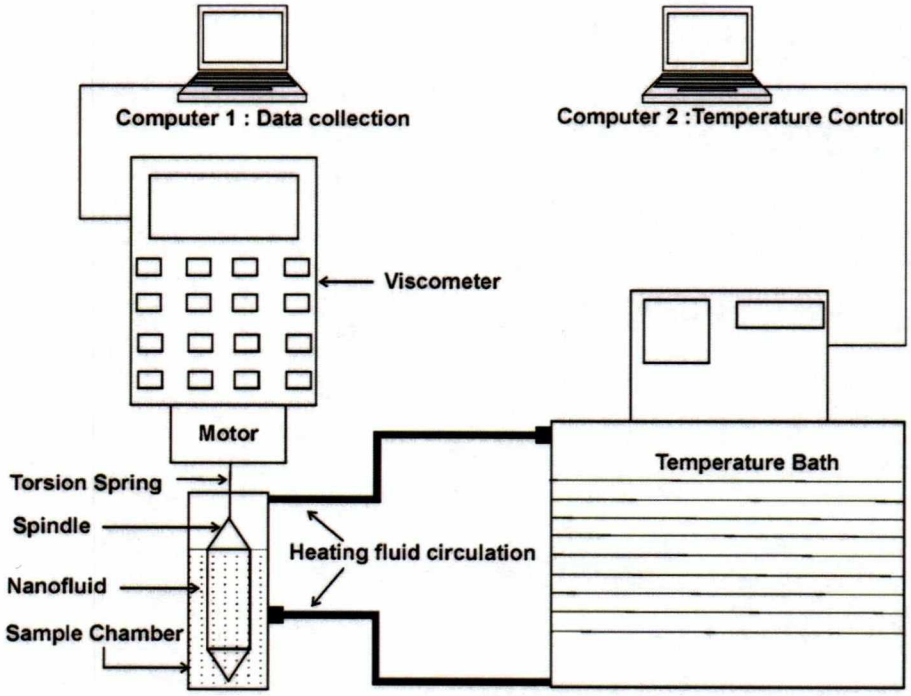

Figure 16: Experimental setup for viscosity measurements at different temperatures (Sahoo et al., 2009)

The setup consists of a Brookfield viscometer, temperature bath, and sample chamber with mounted spindle. To keep the test fluid at its desired temperature, the temperature bath is connected to the viscometer with heating fluid circulation pipes. The viscometer is connected to a computer for data collection, which makes use of WINGATHER software.

The test fluid is then placed inside the sample chamber, and the desired temperature value is adjusted with the temperature bath. Now the spindle rotates with the use of the motor. The number of rotations (RPM) of the spindle was increased for every one set of data. The viscosity measurements are more accurate for torque ranging from 10 to 100%, produced by spindle RPM. For a specific spindle speed, WINGATHER measures the data of torque (%), shear stress (dyne/cm^2), shear strain (1/s), temperature of the test fluid, and time duration of the reading. The relationship between shear stress (τ) and shear strain ( ) is given in Equation 16.

For Newtonian fluids

$$\tau = \mu$$ (16)

Where, μ = viscosity of the sample.

At a specific temperature, a graph is plotted between the shear stress and the shear strain for a torque range of 10 to 100% (shown in Figure 17). The slope of the straight line indicates the viscosity of the fluid.

The entire procedure is repeated at temperatures 0°C, -5°C, and -10°C, and for four different fluids: deionized water, saline water, oil, and antifreeze.

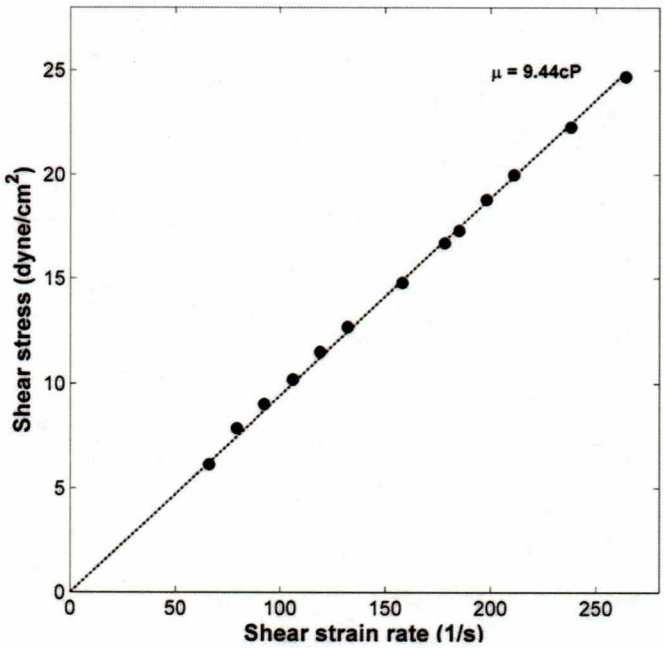

Figure 17: Sample graph between shear stress and shear strain for viscosity measurements of Brookfield calibration fluid (Sahoo et al., 2009)

3.4 Experimental procedure of mercury pycnometer

A pycnometer experiment was used to estimate capillary pressures with respect to wetting phase saturation (air). The average radius of the pores (b) is calculated using the obtained values of capillary pressure. This value of 'b' is then used for the calculation of the radii of ice kernels formed within the pore. The capillary curve generated from the present case is for the drainage process. This experiment was performed on Core 1 at room temperature.

Step 1: Two reference points (upper and lower) had to be set to find the volume of the pycnometer. The lower reference point of mercury was adjusted using a pump piston. The volume of the lower reference point (V_{LR}) was then recorded. The volume of the upper reference point (V_{UR}) was also measured by carefully

advancing the piston. The difference in these two volumes indicates the volume of the pycnometer (V_1).

Step 2: The piston was retracted until the mercury level was at the lower reference point. The dried core sample was inserted inside the pycnometer chamber. The nitrogen valve was then opened with nothing connected to its port, thus opening the pycnometer chamber to atmospheric pressure. The piston was advanced until the mercury level reached the upper reference point. The volume was then recorded (V_2). The bulk volume of the sample (V_b) was calculated in ml by subtracting V_2 from V_1.

$$V_b = V_1 - V_2 \tag{17}$$

Step 3: The pump was retracted to the lower reference point. A pressure, up to 2000 psi, was applied using the control valve of nitrogen gas cylinder. For each incremental increase of pressure applied, mercury penetrates further into the core sample. The new volume of the pycnometer was calculated by advancing the pump piston for each pressure step until the mercury level was observed in the upper reference point. The difference in new volume and the previous pump volume indicates the volume of mercury that has invaded into the core sample at each pressure step.

$$V_{inj} = V_n - V_{initial} - V_{corr} \tag{18}$$

Where,

V_{inj} = The total volume of mercury injected into pores of the core sample since the beginning of the test, measured in ml.

V_n = The pump volume reading in ml, with mercury at the reference level and distinguished at each new pressure step.

$V_{initial}$ = The pump volume reading in ml, with mercury at the same reference level and at beginning pressure with the core sample in the chamber.

V_{corr} = The volume correction (for the expansion of mercury and the cell at that pressure) in ml at each corresponding pressure. The volume is calculated using metal core plugs for each pressure step.

Step 4: Nine different pressure readings were taken by repeating the step 5 at each pressure test.

$$S_g = \left(1 - \frac{V_{inj}}{V_P}\right) * 100\% \quad (19)$$

Where,

S_g = The air (wetting phase) saturation of core sample at each pressure step, as a percent of pore space

V_{inj} = The total (cumulative) volume of mercury injected into the pores of the core samples since beginning the test, at each measured P_c step

P_c = The capillary pressure, psia

V_p = The pore volume of core sample, CC

Step 5: The standard capillary pressure curve of the air–mercury system was obtained by plotting the measured values of P_c in psia on the y-axis, versus the S_g wetting phase saturation in percentage on the x-axis. The capillary pressure data of water-kerosene and kerosene-air were obtained from

$$P_{C_{wk}} = P_{C_{am}} * \frac{\sigma_{wk}}{\sigma_{am}} \quad (20)$$

$$P_{C_{ka}} = P_{C_{am}} * \frac{\sigma_{ka}}{\sigma_{am}} \text{ respectively.} \quad (21)$$

Where,

P_{Cwk} = Capillary pressure of water-kerosene system

P_{Cka} = Capillary pressure of air-kerosene system

P_{Cam} = Capillary pressure of air-mercury system

σ_{am} = Surface tension of air-mercury system = 480 dyne/cm (Dandekar, 2006)

σ_{wk} = Surface tension of water-kerosene system = 48 dyne/cm (Database of

hazardous materials, CAMEO chemicals, 1999)

σ_{ka} = Surface tension of air-kerosene system = 27 dyne/cm (Dandekar, 2006)

Step 6: The radius of the pore was calculated from

$$r = \frac{2\sigma_{am}\cos\Theta_{am}}{P_{C_{am}}} \quad (22)$$

Where,

Θ_{am} = The contacting angle of mercury with the solid surface= 140^0 (Dandekar, 2006).

A total of nine different pressures and saturations were recorded and then plotted against one another. A graph was generated for the air-mercury system as shown in Figure 18. Lower pore size and higher pressure are required for mercury to enter. With less pressure applied initially, the mercury enters the larger pores first; then it moves on to the smaller pores, along with increases in pressure. The transition from larger pores to smaller pores represents the middle portion of the graph. The average radii of the pores of these three zones were considered the average pore radius of the system. Detailed explanations of test procedures and calculations of pore-size distribution are respectively found in Section 3.4 and Section 5.3.

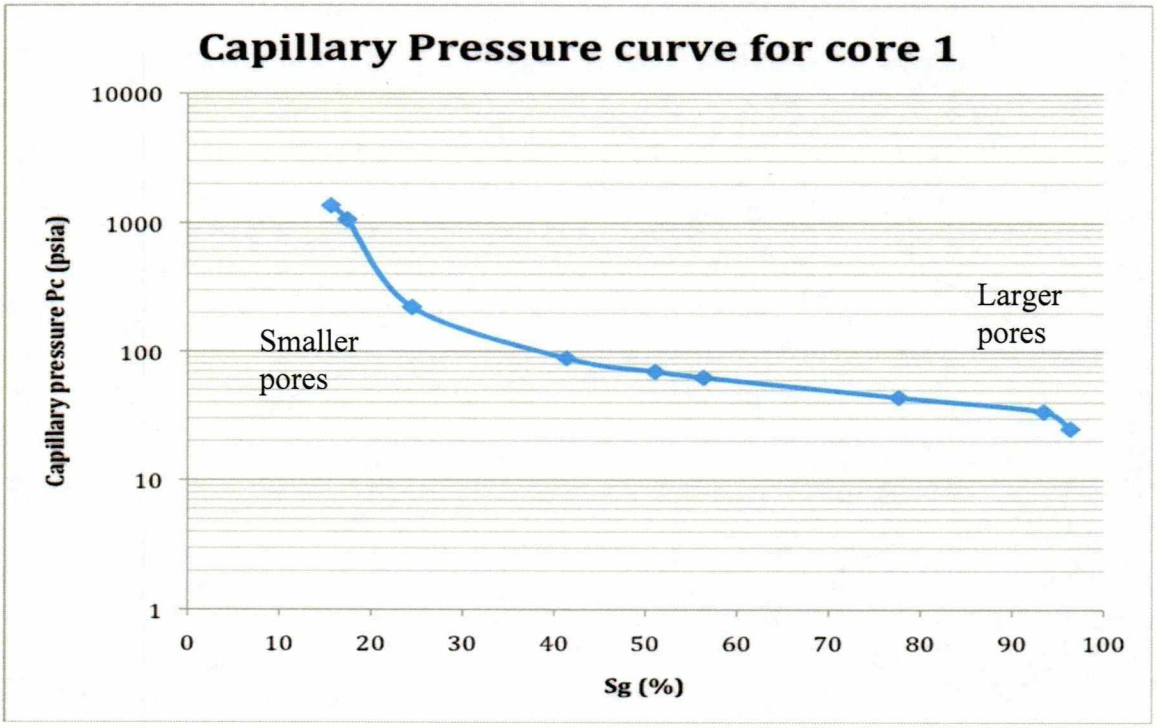

Figure 18: Air –Mercury capillary pressure vs. saturation of wetting phase of Core 1

Detailed calculations of the average radius of the pore, using pore size distribution analysis, are given in Section 5.3.

3.5 Experimental procedure for production technique

Fluids like deionized water (0 ppm), saline water (6467 ppm), and antifreeze (60% ethylene glycol and 40% water) were used for flooding for production of oil from core samples. The core was saturated with water initially as explained in Step 1 of Section 3.2.1. The core was then flooded with the oil (kerosene) sample until the pressure differential (ΔP) across the core stabilized. Next, the core was flooded with the respective flooding fluid until no production of oil was observed. Produced oil was collected in a

volumetric cylinder. This process was repeated for temperatures 23°C, 0°C, -5°C, and -10°C. The collected volume of oil at each temperature was measured and tabulated.

Chapter 4 Theoretical Procedure

Core flooding experiments allow us to observe trends of relative permeability reduction with decreasing temperature and varying salinity. The theoretical approach quantifies the reduction in relative permeability that might be caused by the structural placement of ice. The theoretical approach is an attempt to find the radius of ice formed within the pore space, for three different salinities.

An alternative form of the Kozeny–Carman equation was used in this study to investigate the flow through porous medium. In this euation, effective permeability values are used as inputs to obtain the radius of the ice kernel that is formed in the center of the pore.

The conventional Kozeny–Carman equation is valid for single-phase laminar flow, whereas the alternative form of Kozeny–Carman equation used for this study is governed by several other assumptions. Assumptions and their justifications for the alternative equation are given in the section below.

4.1 Assumptions and their justifications

1) Ice occupies the center of the pore.
   Justification:
   Section 2.4 explains about the Kleinberg (2004) approach using the NMR method. His study indicates that the unfrozen water is in contact with the grain surface, and ice tends to reside in the center of the pore space.

2) The Kozeny–Carman Equation can be used for two-phase flows such as oil and water, and the effective permeability of oil can be used in place of absolute permeability in the calculations.

Justification:

Darcy's law is given as (similar to Equation 6)

$$\frac{\Delta P}{L} = \frac{\mu}{k}\left(\frac{dv}{dt}\right)\frac{1}{A} \tag{23}$$

$$\text{Where } \frac{dv}{dt} = q$$

The Kozeny–Carman equation that has been derived from Hagen-Poiseuille equation for laminar flow is given as (similar to Equation 11)

$$\frac{\Delta P}{L} = \mu\left[\frac{K(1-\varepsilon)^2 S_V^2}{\varepsilon^3}\right]\frac{dv}{dt}\frac{1}{A} \tag{24}$$

Where,

ε = Porosity

S_v = Specific surface

K = Kozeny constant (often 5)

By comparing Equations (23) and (24), the term in the square brackets represents the inverse permeability. This confirms that KC equation (Kozeny–Carman equation) is a subset of Darcy's law.

Musket (1937) proposed two equations on the assumption that Darcy's law is valid for each flowing fluid present in the system.

$$q_g = \frac{kk_{rg}A\Delta P_g}{\mu_g L} \quad and \quad q_l = \frac{kk_{rl}A\Delta P_l}{\mu_l L} \tag{25}$$

In Musket's proposition, kk_{rg} and kk_{rl} are respectively the effective permeabilities of gas and liquid. According to these equations, each fluid phase behaves as a homogeneous system. Since the KC equation is a subset of Darcy's law, the effective permeability can be used in place of absolute permeability (k). In other words, the experimental procedure (Chapter 3) has already stated that the effective

permeability of water at its irreducible water saturation is zero. So, the only significant permeability is the effective permeability of oil, which can be indirectly chosen as the base permeability.

3) Pores are spherical in shape and the average pore radius represents the radius of all pores.

   Justification:

   This is a general assumption and is necessary for the calculation of radius of ice kernel formed.

4) The only mobile phase in the interstices between the pores is oil.

   Justification:

   The effective permeability of oil has been determined using the calculations at irreducible wetting-phase saturation. This means that the mobility of water (wetting phase), at its irreducible saturation, is zero. Assumption 2 thoroughly explains the comparisons between Darcy's law and the Kozeny-Carman Equation. Therefore, in the theoretical approach to the KC Equation, the mobility of unfrozen water has been assumed to be zero. Frozen water is considered as solid phase and its mobility is also zero. This means that upon freezing, the only mobile phase in the interstices of the pore is oil.

5) The pore, pore throats, and the core are assumed to be a system of 'N' pipes in a block.

   Justification:

   Consider that N identical circular pipes of length l and radius b are embedded in a block of length L at an angle α, as shown in Figure 19.

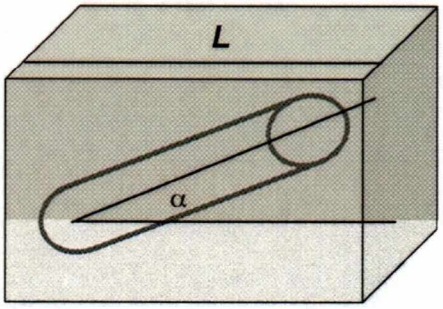

Figure 19: System showing pipe and block network (Dvorkin, J., Personal communication, 2010).

6) Tortuosity has not been changed upon freezing.

   Justification:

   From Figure 19, tortuosity by definition is written as $\tau = \sin^{-1}\alpha = l/L$ (Equation 26). This assumption is necessary for the present model to run; however, this assumption might not be true in the real system. Changes in tortuosity could be expected with the formation ice in the interstices. Considering changes in tortuosity makes the equation more complex and it cannot be solved easily.

4.2 Alternative form of Kozeny – Carman equation

The Kozeny–Carman equation is actually derived from the Hagen–Poiseuille Equation for laminar flow through a circular channel (Chapuis and Aburtin, 2003). This equation was derived for a solid medium with pipe conduits rather than for a granular medium. Dvorkin (personal communication, 2010) proposed an alternative approach for the evolution of the Kozeny–Carman Equation. As proposed by Dvorkin, the derivation of the equation is as follows:

As illustrated in Assumption 5, the system of pore and pore throats is assumed as 'N' pipes embedded in a block. Now, consider the pipe assembly as an absolutely circular open pipe before freezing, then as a concentric pipe with a solid kernel inside the pipe upon freezing. This is shown in Figure 20.

Darcy's Equation is given as

$$Q = -k\frac{A}{\mu}\frac{dP}{dX} \tag{6}$$

Where

Q is the volume flux through the sample (cc/s)

A is the cross-sectional area of the sample (cm^2)

μ is the dynamic viscosity of the fluid (cp)

dP/dx is the pressure drop across the sample divided by the length of the sample (atm/cm).

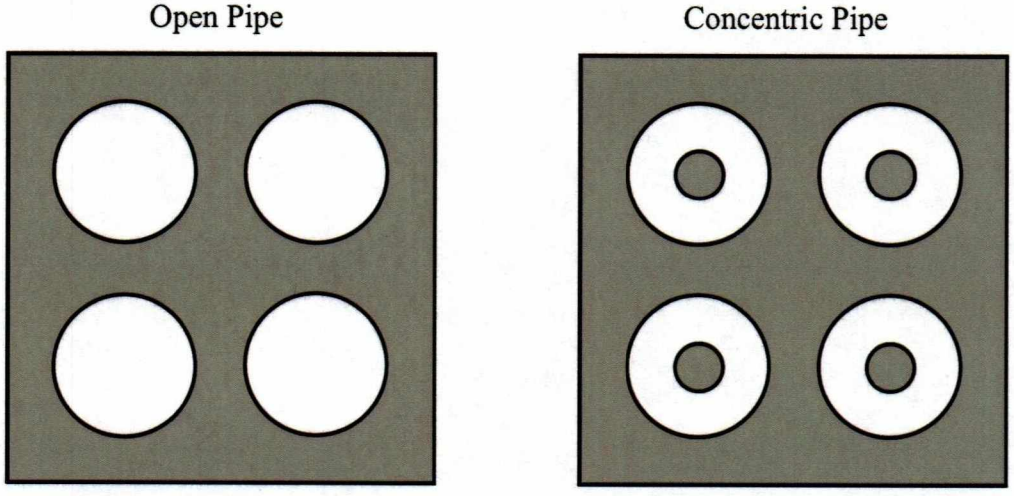

Figure 20: Schematic of open pipe and concentric pipe.

4.2.1 Flow through the circular open pipe (before freezing)

The Equation for the laminar viscous flow in a pipe (Dvorkin, J., Personal communication, 2010) of radius b is

$$\frac{\partial^2 u}{\partial r^2} + \frac{1}{r}\frac{\partial u}{\partial r} = \frac{1}{\mu}\frac{dP}{dx} \tag{27}$$

Where,

u is the velocity of the fluid in the axial (x) direction

$\lceil$ is the dynamic viscosity of the fluid

dP/dx is the pressure gradient in the axial direction

r and x, respectively, are the radial and axial coordinates.

A general solution of Equation (27) is

$$u = \tilde{A} + \tilde{B}r^2 + \tilde{C}\ln r \tag{28}$$

Where,

A, B, and C are constants.

By solving Equation (28),

Differentiating on both sides,

$$\frac{\partial u}{\partial r} = 2\tilde{B}r + \frac{\tilde{C}}{r}, \quad \frac{\partial^2 u}{\partial r^2} = 2\tilde{B} - \frac{\tilde{C}}{r^2} \tag{29}$$

By substituting Equation (29) into Equation (27),

$$2\tilde{B} - \frac{\tilde{C}}{r^2} + 2\tilde{B} + \frac{\tilde{C}}{r^2} = \frac{1}{\mu}\frac{dP}{dy} \tag{30}$$

From Equation (30)

$$\tilde{B} = \frac{1}{4\mu}\frac{dP}{dx} \tag{31}$$

Boundary Conditions,

At r = 0, we take $\tilde{C} = 0$

And at r = b (radius of the pipe), u = 0 (according to fluid mechanics, the fluid is stagnant that is in immediate contact with solid surface)

Then Equation (28) becomes,

$$u = \tilde{A} + \tilde{B}r^2 = \tilde{A} + \frac{1}{4\mu}\frac{dP}{dx} = \tilde{A} + \frac{1}{4\mu}\frac{dP}{dx}b^2 = 0 \tag{32}$$

From the above Equation 24

$$\tilde{A} = \frac{1}{4\mu}\frac{dP}{dx}b^2 \tag{33}$$

By substituting the values of $\tilde{A}, \tilde{B}$ and $\tilde{C}$ in Equation (28)

$$u = -\frac{1}{4\mu}\frac{dP}{dx}b^2\left(1-\frac{r^2}{b^2}\right) \tag{34}$$

Volume flux by definition is q = area * velocity

Therefore, $q = \frac{\pi b^4}{8\mu}\frac{\Delta P}{l}$ (35)

Equation (35) shows the volume flux through a single pipe, but for N identical pipes

$Q = Nq$ (36)

We already know that $l = L\tau$ (from Equation 26)

So, total volume flux is given as,

$$q = Nq = -N\frac{\pi b^4}{8\mu}\frac{\Delta P}{L\tau} = -N\frac{\pi b^4}{8\mu\tau}\frac{dP}{dx} = -N\pi b^2\tau\frac{b^2}{8\mu\tau^2}\frac{dP}{dx} \tag{37}$$

Porosity of N pipes across the block is given by Equation 14,

$\phi = PV/BV$

$PV = N\pi b^2 l$ and $BV = A*L$ (38)

Therefore

$$\phi = \frac{N\pi b^2 l}{AL} = \frac{N\pi b^2\tau}{A} \tag{39}$$

By combining Equation (37) and Equation (39),

$$Q = -\phi\frac{b^2}{8\tau^2}\frac{A}{\mu}\frac{dP}{dx} \tag{40}$$

By comparing Equation (40) and Darcy's law (Equation 6)

$$k = b^2\frac{\phi}{8\tau^2} \tag{41}$$

Also by comparing Equation (37) and Darcy's law (Equation 6)

$$k = \frac{N}{A\tau}\frac{\pi b^4}{8} \tag{42}$$

The final equation for absolute permeability is represented as (from Equation 41 and 42)

$$\boxed{k = b^2\frac{\phi}{8\tau^2} = \frac{N}{A\tau}\frac{\pi b^4}{8}} \tag{43}$$

4.2.2 Flow through the concentric pipe (after freezing)

It is assumed that ice in the form of a solid kernel occupies the center of the pore. Imagine the flow of fluid through a pipe of radius 'b' with a concentric pipe of radius 'a' (radius of ice formed). The equation governing this flow is in the form of Equation (28). This equation with boundary conditions: u = 0 at r = a and r = b is given as (modified from Dvorkin, J., personal communication, 2010)

$$u = -\frac{1}{4}\frac{dP}{dx}b^2\left[\left(1-\frac{r^2}{b^2}\right)-\left(1-\frac{a^2}{b^2}\right)\frac{\ln(b/r)}{\ln(b/a)}\right] \tag{44}$$

Upon integration on both sides, from the definition of volumetric flow rate

$$q = -\frac{\pi}{8\mu}\frac{\Delta P}{l}b^4\left(1-\frac{a^2}{b^2}\right)\left[1+\frac{a^2}{b^2}+\left(1-\frac{a^2}{b^2}\right)\frac{1}{\ln(a/b)}\right] \tag{45}$$

The total flux through N pipes is given as,

$$Q = Nq = -N\frac{\pi}{8\mu}\frac{\Delta P}{l}b^4\left(1-\frac{a^2}{b^2}\right)\left[1+\frac{a^2}{b^2}+\left(1-\frac{a^2}{b^2}\right)\frac{1}{\ln(a/b)}\right] \tag{46}$$

Therefore the permeability is given as

$$k = -\frac{N}{A\tau}\frac{\pi b^4}{8}\left(1-\frac{a^2}{b^2}\right)\left[1+\frac{a^2}{b^2}+\left(1-\frac{a^2}{b^2}\right)\frac{1}{\ln(a/b)}\right] \tag{47}$$

The porosity of the block is

$$\phi = \frac{N\pi(b^2-a^2)l}{AL} = \frac{N\pi(b^2-a^2)\tau}{A} \tag{48}$$

The final Equation for permeability is given as,

$$k = -\frac{\phi}{8\tau^2}b^2\left[1+\frac{a^2}{b^2}+\left(1-\frac{a^2}{b^2}\right)\frac{1}{\ln(a/b)}\right] \tag{49}$$

Equation (35) represents the flow of fluid through the porous media before freezing. Equation (41) represents the flow of fluid through a frozen porous structure. The value of b has been determined using the Mercury Pycnometer experiment, and value of 'a' will be calculated using Equation (41) (for each water sample of different salinity).

Chapter 5 Results

This chapter summarizes the results of core flood experiments on two clean Berea sandstone samples and the theoretical approach to understand the effect of freezing of interstitial water on reductions in relative permeability. A best production strategy for frozen reservoirs is proposed near the chapter's end, reflecting the results of the experiments. The results from the core flooding experiments are used for theoretical calculations. Oil recovery factors are produced in Section 5.5.

5.1 Results of the core flooding experiments

Core flooding experiments (routine core analysis and special core analysis) were carried out at four different temperatures 23°C, 0°C, -5°C and -10°C, and three different salinities 0 ppm (DI), 6467 ppm (Salinity 1) and 5626 ppm (Salinity 2). These experiments were performed with two Berea sandstone cores.

5.1.1 Routine core analysis

The porosity and absolute permeability of two Berea sandstone samples were obtained with routine core analysis experiments (Table 4). Connate water saturation of more than 50% was observed for both cores. The lower irreducible water saturation (Table 4) of Core 2 was due its having higher values of porosity, pore volume, and permeability than Core 1.

Table 4: Results of routine core analysis

Core sample	Pore volume (PV) CC	Porosity (ϕ) %	Absolute permeability (k) md	Irreducible water saturation (S_{wi}) %
Core 1	30.2	18.9	134.1	53.7
Core 2	33.1	20.7	153.3	51.7

5.1.2 Special core analysis

The effective permeability of oil was calculated at three different salinities and four temperatures, as explained in the test procedure. The connate water saturations of Core 1 and Core 2 at the different salinities are given in Table 5. The values of effective permeability for Core 1 and Core 2 are, respectively, listed in Tables 6 and 7.

Table 5: Connate water saturations of Core 1 and Core 2 at different salinities

Core	Connate water saturation S_{wi} (%)		
	DI (0 ppm)	Salinity 1 (6467 ppm)	Salinity 2 (5626 ppm)
Core 1	53.7% ± <1%	50.4% ± <1%	50.4% ± <1%
Core 2	51.7% ± <1%	51.7% ± <1%	51.7% ± <1%

Table 6: Effective permeability data of Core 1

Temperature °C	DI (0 ppm)	Salinity 1 (6467 ppm)	Salinity 2 (5626 ppm)
23	81.2±4.2%	90.5±4.2%	88.1±4.2%
0	67.3±4.2%	87.6±4.2%	87.2±4.2%
-5	48.3±4.2%	74.4±4.2%	66.5±4.2%
-10	46.1±4.2%	60.3±4.2%	55.1±4.2%

Table 7: Effective permeability data of Core 2

Temperature °C	DI (0 ppm)	Salinity 1 (6467 ppm)	Salinity 2 (5626 ppm)
23	87.2±4.2%	93.2±4.2%	89.9±4.2%
0	79.9±4.2%	82.5±4.2%	83.7±4.2%
-5	49.5±4.2%	77.3±4.2%	75.6±4.2%
-10	48.1±4.2%	63.6±4.2%	59.7±4.2%

The "true values" of the above experimental results are expected to fall within the uncertainty range of ±4.2% calculated for the test results. Uncertainty calculation procedure for the experimental data is given in the following section. Detailed calculations for effective and relative permeabilities at different temperatures and salinities are listed in Appendix A.

Relative permeability values for both cores are plotted against temperature in Figure 21.

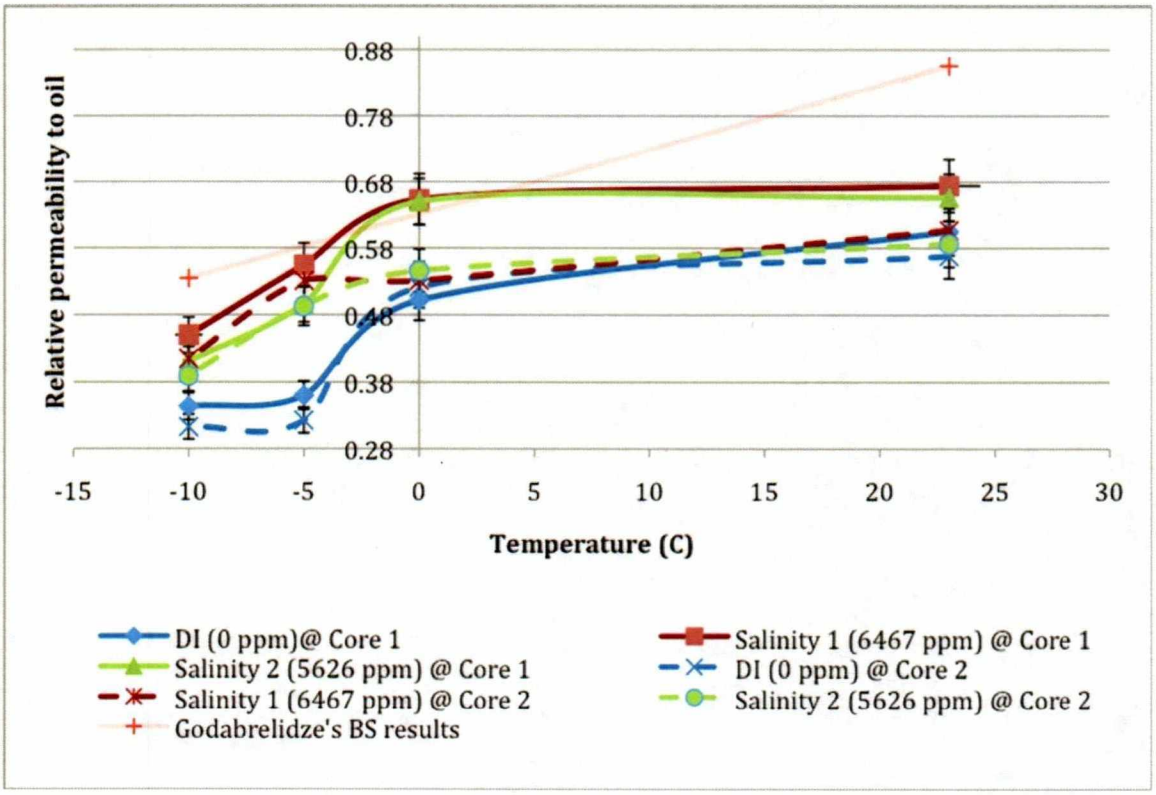

Figure 21: Relative permeability vs. temperature curves of Core 1 and Core 2

To reiterate, the "true values" of relative permeability are expected to fall within the uncertainty range of ±5.94% of the obtained test results.

5.1.3 Effect of temperature on relative permeability

Table 8 presents the percentage decreases in relative permeability with respect to temperature for both of the cores. Because the percentages are derived from the values of relative permeability, the values fall with in the uncertainty range of ±5.94%.

Percentage reductions in the relative permeability to oil were calculated for all three salinities, taking values from 23°C as the reference point (Table 8). All values of relative permeability showed continuous reductions from 23°C to -10°C, although detailed analysis of the effect of temperature below 0°C is still required (Figure 21).

For Core 1, a 40.5% reduction in relative permeability was observed for deionized water at -5°C. With a decrease in temperature to -10°C, a 43.2% reduction was observed. These trends are shown in Figure 21. Factoring in the uncertainty of ±5.94%, we can say that temperature had no significant effect on deionized water in temperature ranges from -5°C to -10°C.

The test at salinity 1 (6467 ppm) showed a reduction of 17.8% (±5.94%) at -5°C and 33.3% (±5.94%) at -10°C (Table 8 and Figure 21). The test at salinity 2 (5626 ppm) showed a reduction of 24.5% (±5.94%) at -5°C and 37.5% (±5.94%) at -10°C (Table 8 and Figure 21). Unlike the test with deionized water, the test with saline water showed a significant reduction in temperature ranges from -5^0C to -10^0C (Figure 21).

Core 2 showed a trend similar to core 1. From -5°C to -10°C, the reduction was just 2% for deionized water, whereas saline water showed a much higher rate of reduction.

Table 8: Percentage reduction in relative permeability to oil with drop in temperature

Core 1			
Temperature °C	**DI**	**Salinity 1**	**Salinity 2**
23	-	-	-
0	17.1%±5.94%.	3.1%±5.94%.	1.0%±5.94%.
-5	40.5%±5.94%.	17.8%±5.94%.	24.5%±5.94%.
-10	43.2%±5.94%.	33.3%±5.94%.	37.5%±5.94%.
Core 2			
23	-	-	-
0	8.3%±5.94%.	12.5%±5.94%.	6.9%±5.94%.
-5	43.2%±5.94%.	12.6%±5.94%.	15.9%±5.94%.
-10	44.9%±5.94%.	31.7%±5.94%.	33.6%±5.94%.

5.1.4 Effect of salinity on relative permeability

The effect of salinity on relative permeability to oil is analyzed in two cases. Case 1 investigates the effect of salinity from 23°C to 0°C, and Case 2 investigates the effect of salinity from 0°C to -10°C.

5.1.4.1 Effect of salinity from 23°C to 0°C

For Core 1, a reduction in relative permeability of 17%, with an uncertainty of 5.94%, was observed for deionized water (Figure 21). For the same temperature range, the reduction was observed to be 3% for salinity 1 (6467 ppm) and 1% for salinity 2

(5626 ppm) (Table 8). Even factoring in error bars, reductions in relative permeability for deionized water were much larger than those for the saline water. This means that relative permeability values of deionized water do not overlap the values of saline water.
Core 2 differs from Core 1 above 0°C, with the trends of all salinities overlapping each other. In relative permeability to oil, deionized water showed a reduction of 8.3% (±5.94%), salinity 1 (6467 ppm) showed a reduction of 12.5% (±5.94%), and salinity 2 (5626 ppm) showed a reduction of 6.9% (±5.94%). Factoring in their error bars, these three salinities overlap each other.

5.1.4.2 Effect of salinity from 0°C to -10°C

For Core 1 at -10°C, a maximum reduction of 43.2% (±5.94%) was observed for deionized water. A minimum reduction of 31% was observed for salinity 1 (6467 ppm) (Figure 21). Core 2 showed a reduction of 44.9% for deionized water and a reduction of 31.7% for salinity 1 (6467 ppm).

5.2 Viscosity changes with temperature

Permeability calculations using Darcy's law (Equation 6) depend on viscosity. The effective permeability values of both cores were calculated using the viscosity of the oil at the corresponding temperature.

The viscosity of the oil (kerosene) was measured with the assumptions and calculations described in the previous chapter. The plot between shear rate and shear strain of oil at -10^0C is given in the Figure 22. The slope of the straight line indicates the viscosity of the fluid. The slope of the graph is 0.0182, which signifies the viscosity of oil in SI units (Poise) at -10^0C. In this way, the viscosity of oil (kerosene) at 23°C, 0°C, -2°C and -5°C was calculated and then plotted (Figure 23).

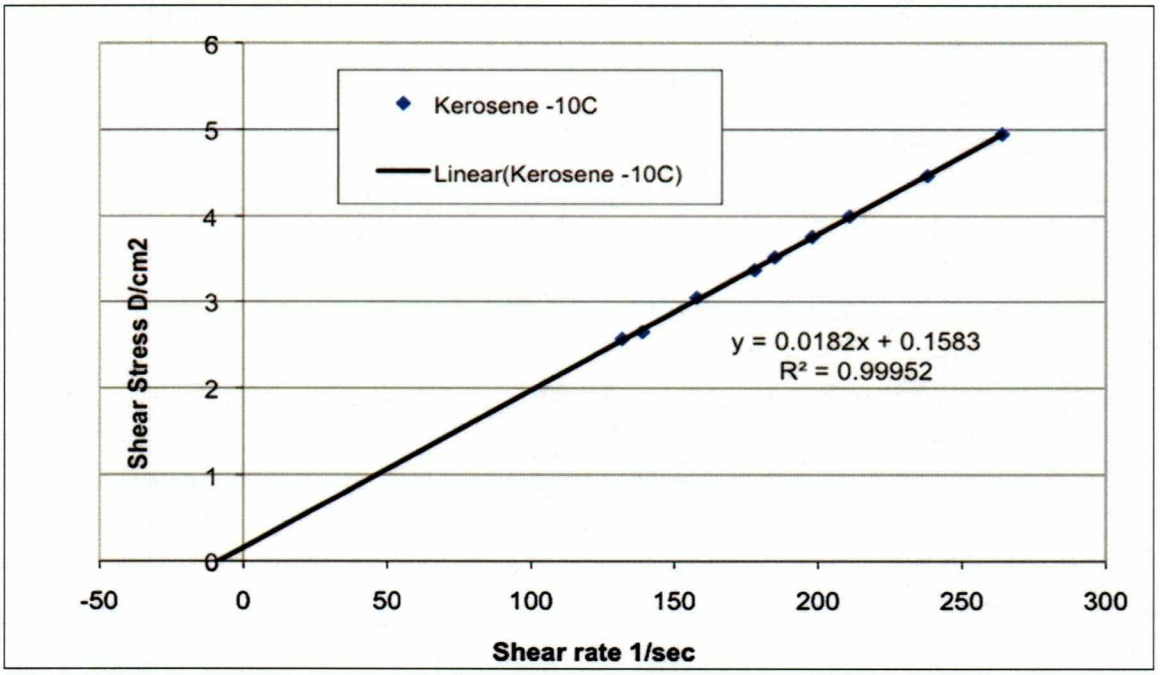

Figure 22: Shear stress vs. shear strain plot for kerosene at -10°C

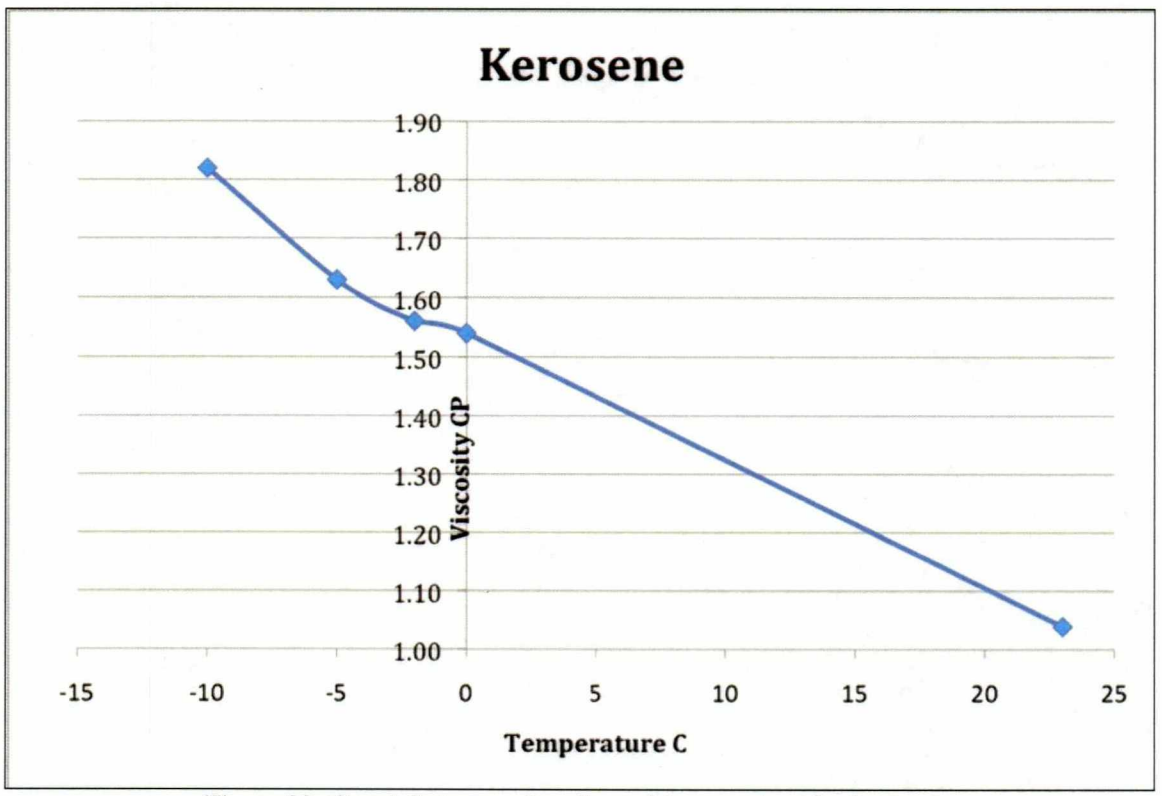

Figure 23: Graph between viscosity and temperature for kerosene

In Appendix B, the remaining shear stress vs. shear strain plots of oil are given, along with three water samples and their viscosity trends with respect to temperature.

5.3 Estimation of freezing point depression

The freezing point depression is the combined effect of the presence of salts and capillary forces. The effect of each parameter is explained in the following sections.

5.3.1 Estimation of depression in freezing point due to salinity

Due to the addition of nine different salts to the pure solvent (water), the final solution had a lower freezing point than pure water. The amount of salt added is shown in Table 3. The depressions in the freezing points of saline water used for this study were calculated using

$$\Delta T_F = K_F \cdot m \cdot i \quad (52)$$

Where,

ΔT_F = Freezing point depression, °C

K_F = Cryoscopic constant, K·kg/mol

For water, K_F = 1.853 K·kg/mol.

m = molality (mol solute per kg of solvent)

i = Van 't Hoff factor (number of ions per mole of solute)

Using Equation 52,

Depression in freezing point of salinity 01, ΔT_F = -1.92°C.

Depression in freezing point of salinity 02, ΔT_F = -1.71°C.

5.3.2 Estimation of depression in freezing point due to capillary pressure

Most substances show an increase in their freezing points when pressure is increased. On the contrary, water shows the reverse behavior of depression in freezing point due to its increase in volume upon freezing. However, the effect of capillary pressure on the freezing point is low. Application of 1450 psi of pressure results in a 1°C shift in the freezing point (Wolfe, 2010). Equation 3 can be used to calculate the depression in the freezing point with various capillary diameters. Table 9 shows the depression in freezing point values at each incremental increase in pressure. The maximum depression in freezing point was observed to be 0.4°C for an application of 1372 psi of pressure.

Table 9: Depression in freezing point due to capillary pressure

Pc air-Hg Psi	Pore radius µm	ΔT_F in K or ^0C
25	3.81	0.007
34	2.76	0.01
44	2.16	0.013
63	1.52	0.019
70	1.37	0.02
89	1.07	0.027
223	0.43	0.07
1067	0.09	0.32
1372	0.07	0.41

5.4 Estimation of pore radius from capillary pressure data

Following the core flooding experiments, a theoretical approach was utilized to examine salinity's effect on reductions in relative permeability when interstitial water is frozen. In order to perform the theoretical analysis, calculation of average pore radius of the core sample was needed. This calculation served as necessary input data for the Kozeny–Carman equation. The radius of the pores of the core sample was calculated from the capillary pressure measurement data.

The capillary pressure data for Core 1 is shown in Table 10 and Figure 24. Table 10 shows the values of gas saturation (air in the present case) inside the core sample, the capillary pressure values of air-mercury (P_{cam}), the water-kerosene (P_{cwk}), and the kerosene-air (P_{cka}). Because the air represents the wetting phase for an air-mercury system, all the curves are for the drainage process. Using a procedure similar to that in Section 5.1.3, the uncertainty of the following pressure values was found to be ±0.25%.

Table 10: Capillary pressure data for core 1

S_g (%)	$P_{c\ air\text{-}Hg}$ (psia)	P_{cwk} (psia)	P_{cka} (psia)
100	14.7	1.47	0.83
96.349	25	2.5	1.41
93.443	34	3.4	1.91
77.619	44	4.4	2.5
56.37	63	6.3	3.5
51.066	70	7.0	3.9
41.346	89	8.9	5
24.491	223	22.3	12.5
17.4	1067	106.7	60.02
15.63	1372	137.2	77.2

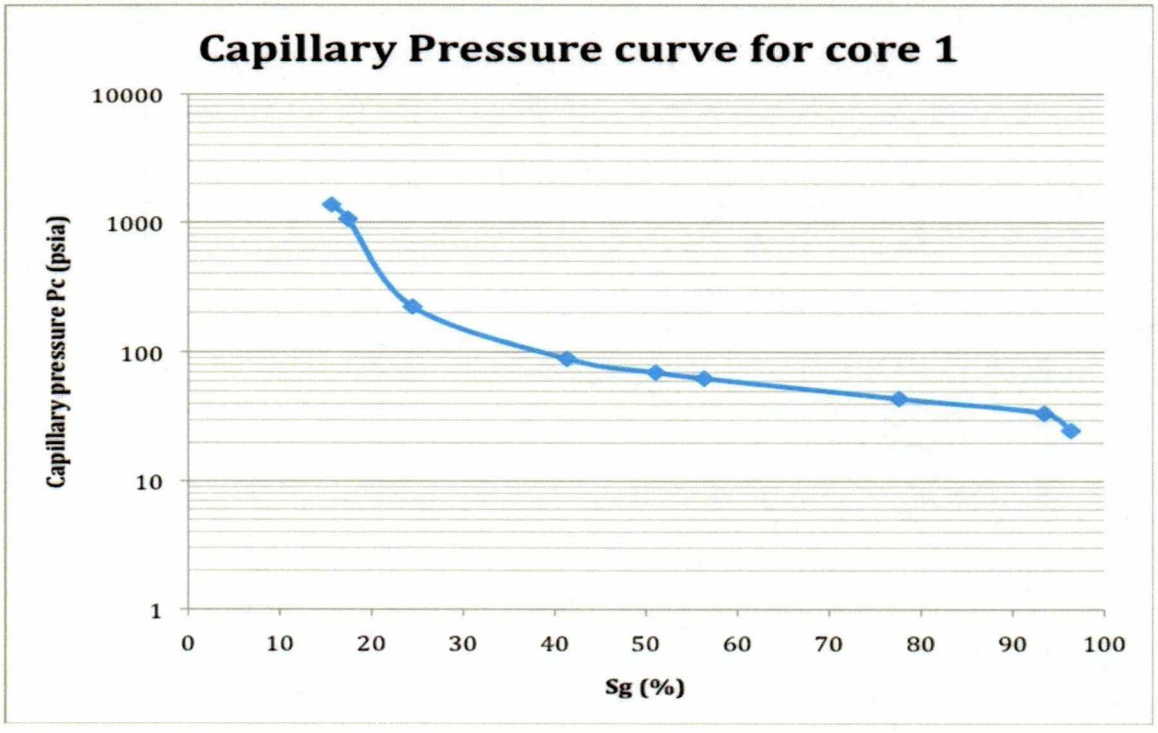

Figure 24: Capillary pressure curve for Core 1 for air-mercury system

The average pore radius can be calculated using the above data. Pores have been classified into large, medium, and small pores according to the pressure applied. In detail, Figure 25 explains the classification of pores with respect to capillary pressure. When low pressures are applied, mercury invades large pores first. Increases in pressure then cause mercury to enter into smaller pores. This phenomenon continues until a breakthrough pressure is achieved, and mercury enters into the smallest-volume pores. Therefore, as the applied pressure increases, the invasion of cumulative volume of non-wetting phase (mercury) into the pores increases. The lower pressure section of Figure 25 displays the large pores of the core sample. With increased applied pressure, the relative size of the pores decreases, indicating the smaller pore region of Figure 25. The transition from larger pores to smaller pores represents the middle portion of the graph.

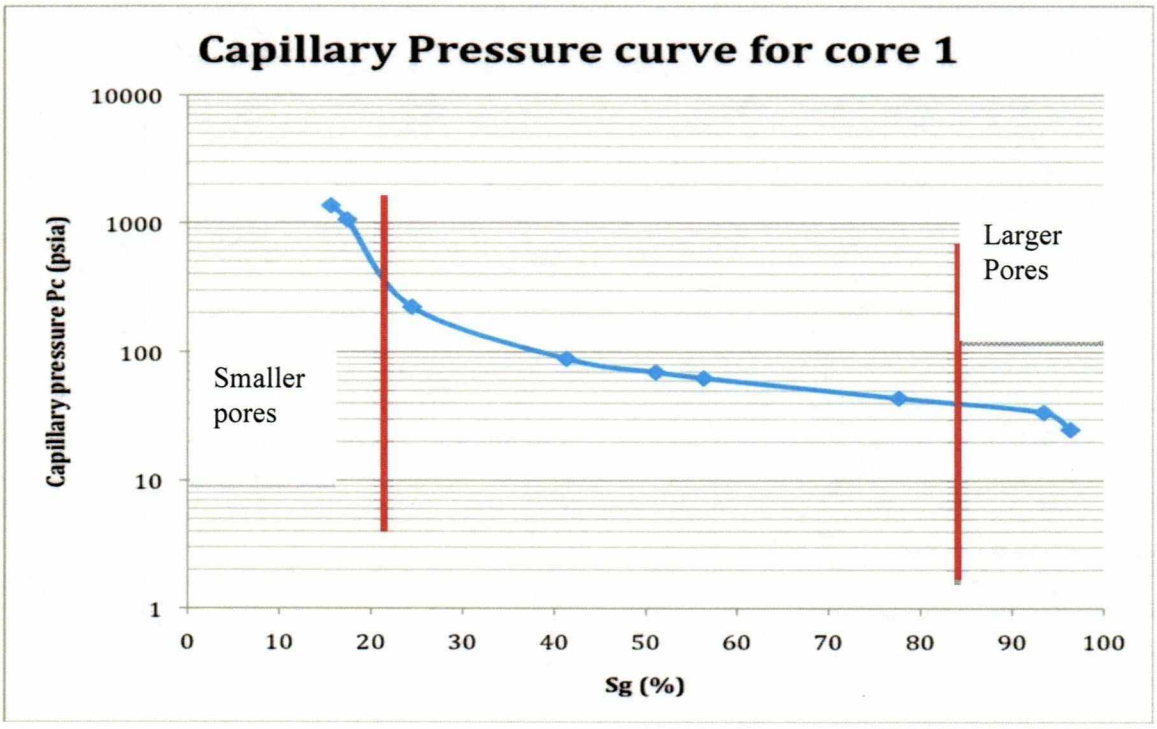

Figure 25: Classification of relative pore size with respect to capillary pressure

A standard method has been followed in the literature to determine pore size. This method consists of the calculation of pore radii at each incremental increase/decrease in pressure applied on the system. The number of pores is proportional to the variations in mercury injected and the corresponding capillary pressure. The radius of the pores can be calculated from Equation 22

$$r = \frac{2\sigma_{am} COS\Theta_{am}}{P_{c_{am}}}$$

Where,

σ_{am}= surface tension of air–mercury and is taken as 480 dynes/cm (Dandekar, 2006)

Θ_{am}= contact angle of mercury against solid and is considered as 140^0 (Dandekar, 2006)

P_{cam} = Applied pressure for air-mercury system.

Figure 26 shows the values of pore aperture radii and pore size distribution.

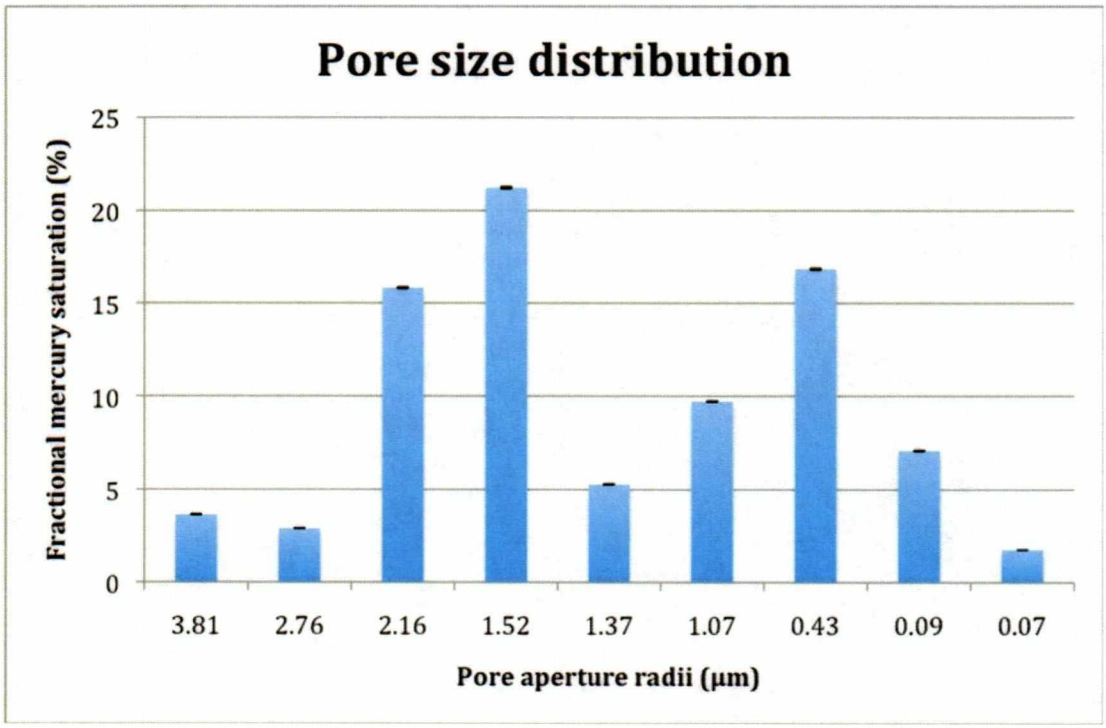

Figure 26: Pore size distribution with error bars for Core 1

The average radius of the pores is considered to be an average pore radius of the core sample. Since pores are occupied by different fractions of volume of mercury, the average is calculated using a volume weighted average method. The volumes of mercury occupied by pore sizes r_1 (0.07μm) to r_9 (3.81μm) are, respectively, V_1 to V_9. The average pore radius is calculated as

$$< r > = \frac{V_1 r_1 + V_2 r_2 + V_3 r_3 + V_4 r_4 + V_5 r_5 + V_6 r_6 + V_7 r_7 + V_8 r_8 + V_9 r_9}{V_1 + V_2 + V_3 + V_4 + V_5 + V_6 + V_7 + V_8 + V_9} \quad (53)$$

Using Equation 53, the average pore radius was calculated to be 1.35 μm ± 0.004 μm.

However, Figure 26 certainly shows a bimodal distribution or a distribution with two distinct modes (Figure 27). The red distribution represents relatively larger pores compared to the blue distribution of Figure 27. Therefore, calculation of the average pore radius of two individual populations is necessary to understand the effect of pore structure on relative permeability to oil. The average size of the larger pores (red

population of Figure 27) calculated from the volumetric weighted average is 1.95 μm ± 0.004 μm and the average size of the smaller pores (blue population of Figure 27) calculated from the volumetric weighted average is 0.63 μm ± 0.004 μm.

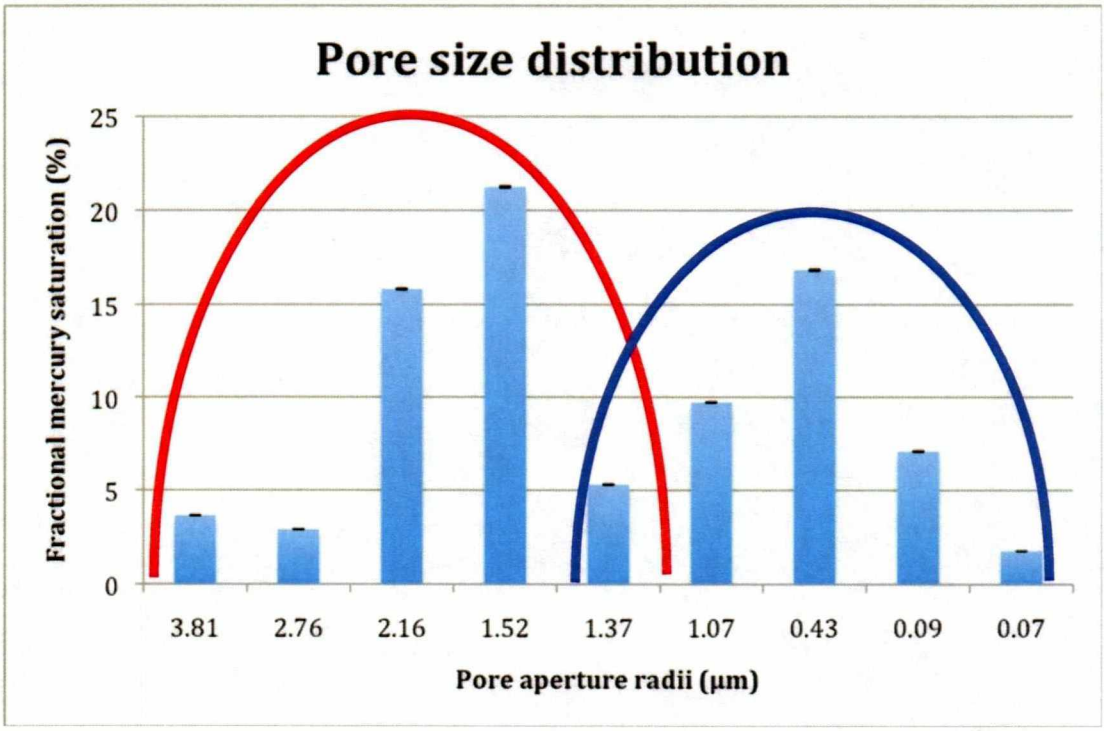

Figure 27: Bimodal distribution of pore sizes for Core 1

5.5 Theoretical approach

An alternative form of Kozeny–Carman equation was used to calculate the radius of ice formed within the pore. Several assumptions were followed as described in Chapter 4.

The KC equation before freezing of interstitial water was given by Equation 43. The KC equation after freezing of interstitial water was given by Equation 49.

Several calculations were made to determine the radii of ice formed within the center of the pore (Appendix C). From the mercury pycnometer experiment, the average

radius of pore (b) was calculated as 1.35 μm (Figure 26). The effective permeability values from the special core analysis were also used as inputs in the equation. The results for the radius of ice kernel formed upon freezing of interstitial water of different salinities at -10°C are listed in Table 11.

Table 11: Radius of ice formed within the center of the pore of Core 1 to corresponding salinity (b = 1.35 μm)

Salinity (ppm)	Radius of ice kernel formed within the center of the pore (μm)
0	0.145 ± 0.004 μm
5626	0.098 ± 0.004 μm
6467	0.069 ± 0.004 μm

As observed in Table 11, the size of ice formed within the center of the pore decreased as salinity increased in the water sample. At 6467 ppm salinity, a 50% reduction was observed in the size of the ice kernel that formed within the center of the pore as compared to the one in deionized water.

Table 11 represents the radius of the ice formed in the center of the pore considering all the pores have same radius of 1.35 μm. However, the two populations of Figure 27 shows two distinct sizes of pores. Therefore, radius of ice formed in the center of the pore is also calculated for both populations (red and blue populations of Figure 27) and are tabulated (Table 12 and Table 13).

Table 12: Radius of ice formed within the center of the pore of Core 1 to corresponding salinity (red population and b = 1.95 μm)

Salinity (ppm)	Radius of ice kernel formed within the center of the pore (μm)
0	0.21 ± 0.004 μm
5626	0.1 ± 0.004 μm
6467	0.142 ± 0.004 μm

Table 13: Radius of ice formed within the center of the pore of Core 1 to corresponding salinity (blue population and b = 0.63 μm)

Salinity (ppm)	Radius of ice kernel formed within the center of the pore (μm)
0	0.068± 0.004 μm
5626	0.032± 0.004 μm
6467	0.046± 0.004 μm

Effects of these distinct pore sizes on relative permeability to oil are discussed in section 6.2.2.3.

5.6 Results of production mechanism

Because the freezing of interstitial water is one reason for reductions in productivity when producing from frozen reservoirs, investigation into a better production mechanism is needed. In order to achieve maximum recovery in the field, different fluids for flooding were tested. Deionized water, saline water, and antifreeze

(60% ethylene glycol (EG) + 40% water) were used as injection fluids for the core sample.

As presented in Table 4, the total pore volume of Core 1 is 30.25 CC, with 53.7% connate water saturation. Therefore, the volume of oil in the pores is 14 CC. Core 2 has 16 CC of oil in its pores. For each fluid tested, recovery factors were calculated based on the amount of oil recovered with respect to total oil saturation of the pore volume. Table 14 and Table 15 show the results of the recovery of oil, with corresponding flooding fluid for Core 1 and Core 2, respectively. The error in measuring the oil volume collected was 0.1 CC, which was the standard error for the cylinder that collected produced oil.

Table 14: Recovery of oil (CC) for Core 1

Flooding fluid	**Temperature**			
	23°C	**0°C**	**-5°C**	**-10°C**
	Recovery factor	**Recovery factor**	**Recovery factor**	**Recovery factor**
Deionized water	0.78	No Production	No Production	No Production
Saline water (6467 ppm)	0.78	0.57	No Production	No Production
Antifreeze (60% EG +40% water)	Experiments were not conducted	0.67	0.57	0.5

Table 15: Recovery of oil (CC) for Core 2

Flooding fluid	Temperature			
	23°C	**0°C**	**-5°C**	**-10°C**
	Recovery factor	**Recovery factor**	**Recovery factor**	**Recovery factor**
Deionized water	0.62	No Production	No Production	No Production
Saline water (6467 ppm)	0.62	0.5	No Production	No Production
Antifreeze (60% EG +40% water)	Experiments were not conducted	0.62	0.5	0.31

Discussion of effect of temperature, salinity on relative permeability trends and determination for the best production techniques are detailed in Chapter 6.

Chapter 6 Discussion

6.1 Routine core analysis

Irreducible water saturation of more than 50% was observed due to the unstable displacement characteristic of kerosene. The kerosene used in the experiment had low viscosity at room temperature (Figure 23), too low to adequately push the water out of the core sample. Thus, the irreducible water saturation showed a higher value than it normally would.

6.2 Relative permeability measurements

Figure 21 shows the relative permeability to oil behavior with respect to temperature and salinity. Irrespective of salinity, the results of special core analysis show reductions in relative permeability to oil as the temperature shifts from 23°C to -10°C. The relative permeability behavior can be discussed in terms of above zero and below zero behavior.

6.2.1 Relative permeability to oil above 0°C

Figure 21 illustrates that, regardless of salinity, the relative permeability to oil decreases with temperature from 23^0C to 0^0C. The possible reasons for this reduction could be the changes in viscosity of oil (kerosene for this study) and interfacial tension (IFT). Both viscosity and IFT increase as the temperature drops. Therefore, reductions in relative permeability can be attributed to increases in viscosity and IFT. However, the effect of viscosity is already accounted by the values of increased viscosity in Darcy's equation used to calculate relative permeability. The main parameter is the IFT, which

could be the reason for reductions above 0°C. As the IFT increases, the water and oil phases become less mobile, resulting in poor values of relative permeability to oil.

As discussed in Chapter 5 (Section 5.1.5), another anomalous behavior that needs to be addressed is the relative permeability values of the deionized water of Core 1 (Figure 21). The reason for divergence of the curve of deionized water with the values of saline water can be explained by core's irreducible water saturations. Table 5 shows the values of connate water saturations of different salinities. For Core 1, S_{wi} of saline water is 50.7%, whereas S_{wi} of pure water is 53.7%, which indicates the increased mobility of oil phase in the case of saline water. Thus, the relative permeability to oil values for saline water were more than those for deionized water. Therefore, relative permeability values in case of deionized water did not overlap with the relative permeability values for saline water (unlike Core 2). Core 2 has the same connate water saturations for all salinities.

6.2.2 Relative permeability to oil below 0°C

Experimental data indicate that the relative permeability to oil decreases with decreasing temperature (Figure 24), particularly below 0°C. The cause for this reduction in relative permeability could be a function of parameters other than just temperature. The first parameter that could cause a reduction is an increase in viscosity with decrease in temperature. However, the value of increased viscosity due to drop in temperature is added to the Darcy's Equation when calculating relative permeability to oil. Consequently, the effect of viscosity on reductions in relative permeability is nullified.

Other parameters that could affect relative permeability, particularly in frozen reservoirs, are fluid saturations, formation water salinity, capillary pressure, and pore structure. These parameters will be discussed individually in the following sections.

6.2.2.1 Effect of water saturation

The first parameter that could alter relative permeability to oil directly is fluid saturation. Relative permeability is a direct function of saturation. If the wetting phase (water) saturation increases (imbibitions), relative permeability of that phase increases as well, and relative permeability of the non-wetting phase (oil) decreases. In this study, relative permeability measurements were carried out at irreducible water saturations for all of the temperatures. Other investigators (Raymond, 1979; Narahara et al., 1993) have stated in the literature that water saturation has no effect on water-oil relative permeabilities as long as the water is immobile. However, water saturation did affect the relative permeability in a frozen reservoir, though the measurements were carried out at irreducible water saturation.

Saturation is a direct function of volume of that phase. As water freezes, its volume increases by 10 percent. The volume of the ice phase determines the increase or decrease in relative permeability to oil.

Frozen water does not continue to deform under the application of shear stress, which is an essential fluid property. Therefore, frozen water (i.e., ice) is considered as a separate solid phase. Ice within the pores results in reduced pore volume eventually increasing the water saturation. Since water saturation would increase due to the increase in volume of pore space occupied by water, the non-wetting phase saturation (oil) decreases. However, relative permeability to oil would increase due to the overall decrease in pore volume.

6.2.2.2 Effect of salinity and capillary pressure

Three different salinities were used for core flooding experiments (Figure 24). Pure water freezes at 0°C. The presence of salts and capillary pressures alter this freezing point, most often decreasing it. The higher the salinity, the lower the freezing point. Capillary forces that exist in pores further decrease the freezing point of saline waters.

Maximum depression in the freezing point due to capillary forces is observed to be 0.4°C (Section 5.3.2). The combination of these two effects, salinity and capillary forces, results in the existence of unfrozen water in pores and pore throats even when temperatures are well below °C. Theoretical analysis promises to advance understanding of the effect of freezing of interstitial water on relative permeability to oil.

From Table 11, it is evident that water with 6,467 ppm salinity has less frozen water in the pore space than does deionized water. Hence, pores saturated with saline water possess higher quantities of unfrozen water compared to pores saturated with deionized water. This is due to the depression of the freezing point of water caused by the presence of salts and capillary forces. Ice resides in the pore space and in the pore throats and acts like a solid boundary, which results in obstruction of flow by narrowing the net flow path. The scale of obstruction is more if the connate water is less concentrated with salts. As the salinity of formation water increases, it provides greater passage for the flow of fluids through the reservoir's pore network. Therefore, salinity of the formation water is also one of the reasons for reductions in relative permeability to oil below 0°C.

In this study, water with 6467 ppm salinity has a higher freezing point depression than does water of 5626 or 0 ppm salinity. The freezing point of 6467 ppm salt water was calculated to be -1.92°C. The freezing point of water with 5626 ppm salinity was -1.71°C. Further maximum depression in the freezing point due to capillary pressure was 0.41°C (Section 5.3.2). As a result, theoretically (considering algebraic sum), a rock saturated with water should be totally frozen between -2.3°C for 6467 ppm salinity and -2.1°C for 5626 ppm salinity. The maximum reductions in relative permeability should be observed at those temperatures for the respective salinities, but in contrast, we observed continuity in reductions even below the freezing temperatures (Figure 21). This phenomenon indicates the presence of unfrozen water even below the freezing point of the in situ water. A possible reason for this could be that water freezes first at the center of the pore, expelling salts that may exist in the pore water. This causes unfrozen water closer to the particle surfaces to have a higher concentration of salts than previously

existed and a lower freezing point. Consequently, the entire pore water doesn't necessarily freeze, leaving certain quantities of unfrozen water.

6.2.2.3 Effect of pore structure

In general, rocks with large pores have low irreducible water saturations and therefore a relatively large amount of pore space available for the flow of fluids. This condition allows high relative permeability end points to exist. Correspondingly, rocks with small pores have high irreducible water saturations that leave little room for the flow of hydrocarbons. This condition creates low values of oil relative permeability.

The outer concentric circle represents size of the pore and the inner concentric circle of Figure 28 represents the size of the ice. Table 11 represents a model that is represented in Figure 28 A. In this model, all the pore sizes are equal and the size of the ice formed in the center of the pore solely depends on its salinity (Figure 28 A). However, pores of the Core 1 are actually represented by two distinct sizes (Figure 27) and, according to theoretical calculations, would result in the distribution of ice kernels as shown in Figure 28 B. This variation in pore sizes within the reservoir rock would certainly influence the relative permeability to oil.

In a frozen reservoir, larger pores are occupied by ice, leaving only a narrow path for the flow of fluids. Early freezing of water in larger pores is mostly due to lower values of capillary pressure (Figure 28 B). This results in lower values of relative permeability. Smaller pores tend to be ice free due to their higher capillary pressures. Moreover, pore throats are certainly smaller in size compared to the average pore size obtained from capillary measurements. These pore throats are also occupied by unfrozen water. Consequently, the relative permeabilities obtained are of a lower magnitude.

As seen from Figure 28 B, large pores of Core 1 are more likely to contain ice as compared to small pores. This is due to the lower capillary pressures in the larger pores. Ice in the larger pores tends to obstruct the flow of fluids. In contrast, smaller pores are

occupied by less ice (or perhaps no ice) due to extremely higher values of capillary pressure.

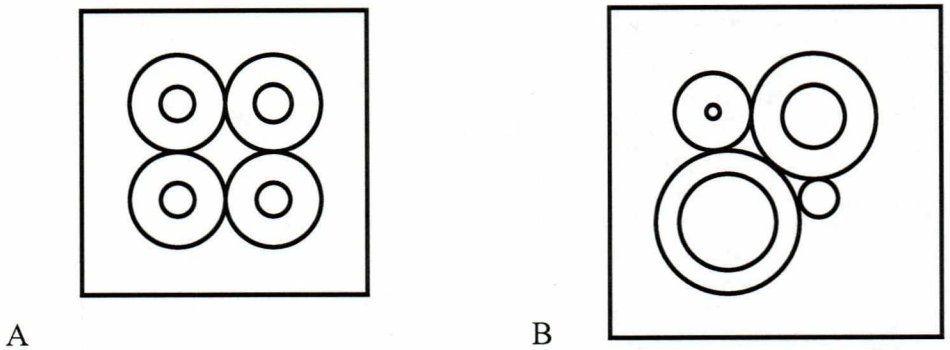

Figure 28: Schematic of different sizes of pores and their respective sizes of ice formed at the center A) Size of ice formed in the pores of equal size B) Size of the ice formed in the pores of different sizes.

6.2.2.4 Summary

Though the changes in fluid saturation purely due to the presence of ice, should result in an increase in relative permeability to oil (Section 6.2.2.1), the combined additional influence of salinity and capillary pressure (Section 6.2.2.3), and the pore structure (Section 6.2.2.3) would result in overall reduction in relative permeability to oil.

In summary, a number of factors influence the relative permeability to oil in a frozen reservoir: water saturation, salinity, capillary pressures, and pore sizes. All factors must be considered when analyzing the oil relative permeabilities of a frozen reservoir.

6.3 Production mechanism

The Umiat reservoir is located in shallow depths of 275 ft to 1,100 ft and has very low reservoir pressure of 50 psi to 350 psi (Baptist, 1960). The Umiat reservoir is an under saturated reservoir with no aquifer support. Literature states that the pressure

support for primary production was supplemented by solution gas drive mechanisms (Watt et al., 2010). However, this might not be the sole reason for primary production. Recovery factors of 29% to 45% (Baptist, 1960) could not be achieved solely by expansion of small amount of gas in the solution. According to the critical observations of this study, external pressure support such as gas injection or water flooding is mandatory to produce from the low pressure reservoir. A lack of aquifer support and poor pressure support of the reservoir make the search for a best production mechanism necessary.

Secondary recovery techniques are required to optimize field development and production from low-pressure frozen reservoirs. One assumes that keeping the formation cold and stable would result in higher recoveries than to thaw and refreeze the formation through water injection. Based on this assumption, cold gas injection has been suggested by the U.S. Bureau of Mines as a secondary recovery mechanism in frozen reservoirs.

The common belief is that water injected into the formation tends to freeze and block the formation from further injection. Similarly, either gas or water injected above reservoir temperatures (hot injection gas or water) tends to thaw then refreeze interstitial water, which results in blockage of pores. Therefore, cold gas injection can be considered for secondary recovery mechanism. Moreover, the abundance of gas on the North Slope also supports the idea of cold gas injection.

One of the challenges of a frozen formation is that its ice resides in the center of pores. Minimizing the blockage of pores due to freezing of in situ water may resolve the problem of poor recovery, as stated by Baptist (1960). One aspect of the present study focused on production techniques using fluids other than cold gas. Fluids like deionized water, saline water (6456 ppm), and antifreeze (60% ethylene glycol or propylene glycol + 40% water) were used as flooding fluids for secondary recovery.

The performance of these flooding fluids and recovery factors are shown in Table 14 and Table 15. No production was observed in the case of deionized water for Core 1 and Core 2 at temperatures below 0°C. This is solely because of freezing of the interstitial water. The idea of melting the existing in situ ice and keeping the formation fluids

unfrozen might result in good recoveries. Consequently, saline water was tested as a flooding fluid. Adding salts decreases the freezing temperature. The melting point of the ice, however, is unchanged by the presence of these foreign materials, so melting occurs at a higher temperature than freezing. When saline water was tested as a flooding fluid, 57% of oil was recovered at 0°C. This was due to the higher temperature brine melting the ice existing within the pores. When ice melts, a larger space becomes available for the flow of fluids. In addition, unlike deionized water, saline water does not freeze while flowing within the interstices of the reservoir. The higher viscosity value of this saline water as compared to deionized water at 0°C could be useful in better recovery of oil.

Depending on its salinity, saline water helps to keep interstitial water unfrozen until a certain temperature. This suggest saline water as an injection fluid for frozen reservoirs that have subsurface temperatures near 0°C. However, what is an appropriate flooding fluid for frozen reservoirs that have temperatures much lower than 0°C?

Further increase in the salinity concentration of salinity might be the answer. However, the selected concentration and components of the saline water must be a close match with the formation–water salinity. Otherwise, this might cause an exchange of ions between the formation and injection saline water and result in a zone of low or zero salinity. This could result in blockage of pores due to interstitial water freezing (Weatherford laboratories)

Flooding with antifreeze is another option. From Tables 14 and 15, it is clear that when antifreeze was used as a flooding fluid, the reservoir produced, even at temperatures significantly lower than 0°C. At -10°C, we can see recovery rates of 50% and 31%, using 60% ethylene glycol + 40% water, respectively for Core 1 and Core 2 (Table 14 and Table 15). 60% propylene glycol/40% water is another antifreeze that could be used for flooding, but was not tested in these experiments.

Similar to saline water, these fluids melt the existing ice within the interstices and also keep the fluids unfrozen throughout the flooding process. These fluids provide a freer channel for the flow of fluids through the pores and pore throats by melting the frozen interstitial water. Water will not refreeze while these fluids reside in the formation.

These two fluids (60% ethylene glycol or propylene glycol and 40% water) are relatively cheap at $0.50-$0.90/lb (www.icis.com). They also possess a lowest freezing point of -54°C and can be considered best for flooding techniques.

The viscosity of these fluids is a major factor in determining the best production strategy. Viscosity profiles with respect to temperature of the ethylene mixture and propylene mixtures are shown in Figure 29.

The propylene glycol mixture showed a higher value of viscosity at low temperatures than the ethylene glycol mixture. Higher viscosity of propylene glycol mixture results in better flooding capability than does the ethylene glycol mixture. However, high-powered machinery certainly would be required to pump the propylene glycol mixture into the formation. On the other hand, the viscosity of ethylene glycol may be low enough to pump in a more cost-effective way. Disregarding pumping costs, the low cost of these mixtures and their ability to replace oil even at -10°C, make them better flooding fluids that should be considered as best production strategy for frozen reservoirs.

Baptist (1960) showed a recovery of 20% to 34% at -3°C using gas drive as a recovery technique (Table 2). These figures are for the core samples that had permeabilities greater than 100 md. The present study of production mechanisms showed nearly 50% recovery using saline water, and 60% recovery using antifreeze (60% ethylene glycol+40% water) at -5°C for both cores. Additional production is also observed at -10°C with a recovery factor of 50% for Core 1 and 30% for Core 2. The main aim of these production strategy experiments was to explore the use of water injection, in the hope of using saline water as a flooding fluid (depending on formation temperature). Saline water could possibly melt the frozen interstitial water and provide higher recovery factors than those of cold gas injection. Thus, it is advisable to invest in saline water injection if the produced oil through water injection generates more revenue than cold gas injection. However, the selection of a liquid for water injection is determined by ever-changing petroleum production economics.

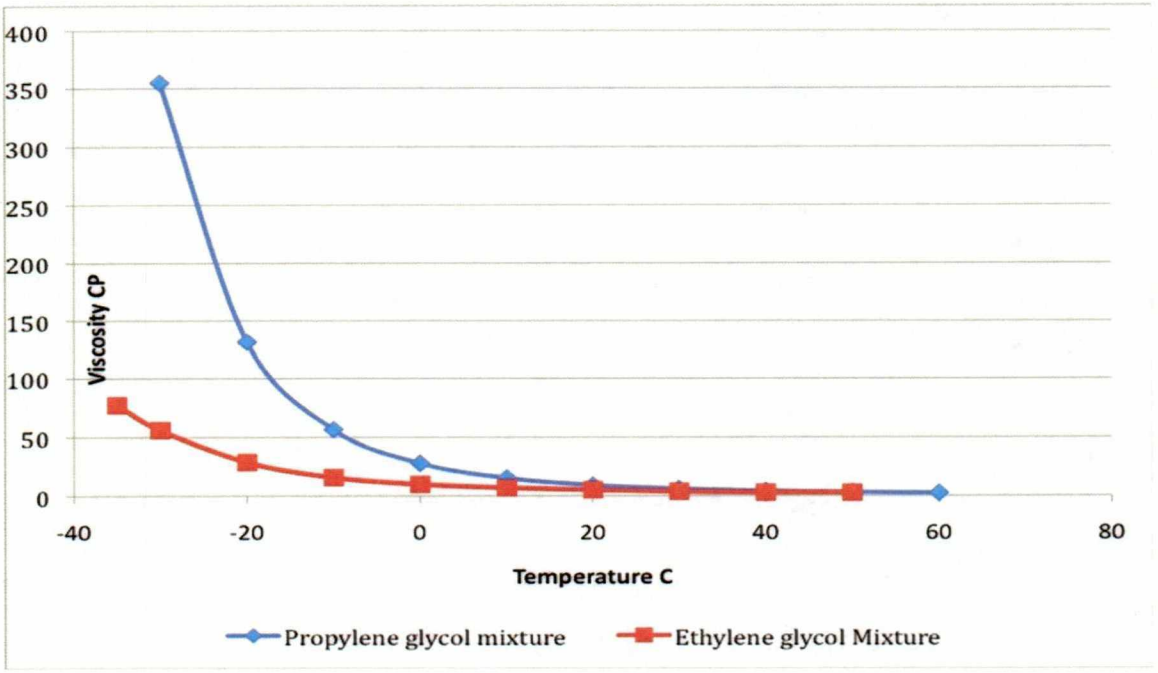

Figure 29: Viscosity vs. temperature profiles for a mixture of 60% ethylene glycol and 40% water and mixture of 60% propylene glycol and 40% water (Sahoo et al., 2009)

Chapter 7 Conclusions and Recommendations

The main aims of this study were to investigate the reasons for reduction in relative permeability to oil in a frozen reservoir rock and to propose a possible production mechanism. Core flooding experiments were performed on two clean Berea sandstone samples to examine the behavior of relative permeability with respect to temperatures 23°C, 0°C, -5°C, and -10°C and salinities of 0 ppm, 6467 ppm, 5626 ppm. Several fluids were tested as potential flooding fluids for the core sample at permafrost conditions.

7.1 Conclusions

Continuous reduction in relative permeability was observed for both cores with reduction in temperature from 23°C to -10°C for all three salinities. As the temperature was decreased to -10°C, Core 1 showed maximum reduction of 43.2% in relative permeability to oil when saturated with deionized water and showed a minimum reduction of 33.3% when saturated with 6467 ppm of saline water. Core 2 showed maximum reduction of 43.2% relative permeability to oil when saturated with deionized water and showed a minimum reduction of 31.7% when saturated with 6467 ppm of saline water.

Theoretically, the radius of ice formed in the center of the pore can be determined using a Kozeny-Carman equation and pore sizes derived from mercury capillary pressure experiments. In the Berea sandstone samples used in this study, the size of ice kernels residing in the center of pores decreased with increasing salinity. At -10°C, the radius of ice dropped from 0.145 μm to 0.069 μm when flooding water salinity was increased to 6467 ppm. This result was consistent with experimental results, where higher salinities of in situ water resulted in lower reductions in relative permeability when the samples were frozen.

This study suggests that a variety of factors influence the relative permeability to oil in frozen reservoirs, including changes in water saturation due to freezing of

interstitial water, depression in freezing point due to formation salinity and capillary pressure, and different pore sizes of the host rock.

Fluids like deionized water, saline water, and antifreeze (a mixture of 60% ethylene or propylene glycol with 40% water) were tested to find the best flooding agent for frozen reservoirs. At 0°C, 9% greater recovery was observed with antifreeze than with saline water. Antifreeze showed 48% total recovery even at -10°C, at which temperature the rest of the fluids (deionized water and saline water) failed to increase production. In this study, a mixture of 60% ethylene glycol (or propylene glycol) and 40% water was found to be the best flooding fluid.

7.2 Recommendations

- NMR experiments are strongly recommended to further investigate the structural placement of ice within the pores and for accurate estimation of unfrozen water content of reservoirs under freezing conditions.
- Even though the effects of the freezing of interstitial water on relative permeability are examined here, the effect of interfacial tension on relative permeability due to decrease in temperature needs to be addressed.
- Pore scale modeling of a frozen reservoir rock could be an efficient addition to this experimental work and would improve our understanding of the fundamental flow behavior within a frozen reservoir rock and help in the prediction of properties like relative permeability and capillary pressure.
- A detailed simulation study of fluid behaviors and fluid-ice interactions of frozen reservoirs using software like COMSOL would be useful.
- Investigation of solutes that could possibly reduce the interfacial tension between the fluids of the frozen reservoir is necessary. Adding these solutes to the injection fluids would possibly increase production.

- Flooding with different saline waters of a wider range in composition and concentration would probably result in better recovery than that detailed in the study.

References

'ajm' petroleum consultants (2011). In differentiating conventional oil versus unconventional oil chart. Retrieved February 16 2011 from www.ajmpc.com.

Alboudwarej, H., Felix, J., Taylor, S., Badry, R., Bremner, C., . . . West, C., (2006). Highlighting heavy oil. Retrieved July 15, 2011 from http://www.slb.com/~/media/Files/resources/oilfield_review/ors06/sum06/heavy_oil.ashx.

Anderson, D.M., Tice, A.R. (1971). Low-temperature phases of interfacial water in clay–water systems. Proceedings - Soil Science Society of America, 1971, 35, 47 – 54.

Anderson, R., Llamedo, M., Tohidi, B., Burgass, R.W. (2003). Experimental measurement of methane and carbon dioxide clathrate hydrate equilibria in mesoporous silica. The Journal of Physical Chemistry B, 2003, 107, 3507–3514.

Baptist, O.C. (1960). Oil Production from Reservoir Rocks, Umiat, Alaska. SPE-1219-G.

CAMEO chemicals. (n.d). Database of hazardous materials. Retrieved April 27, 2010 from www.cameochemicals.nova.gov.

Carman, P.C. (1937). Fluid flow through granular beds. Transactions, Institution of Chemical Engineers, London, 15, 150-166.

Chapuis, R.P., Aburtin, M. (2003). Predicting the coefficient of permeability of soils using the Kozeny–Carman Equation. Department CGM, Ecole Polytechnique de Montreal.

Christ, M., Kim, Y. (2009). Experimental Study on the Physical-Mechanical Properties of Frozen Silt. KSCE Journal of Civil Engineering, 13(5), 317-324.

Coleman, H.W., Steele, W.G. (2009). Experimentation, Validation, and Uncertainty Analysis for Engineers, 3rd edition. New Jersey, NJ: John Wiley and Sons.

Collins, F.R. (1958). Test wells, Umiat area, Alaska. U.S. Geological Survey Professional Paper, 305-B, p. 71-206.

Dandekar, A.Y. (2006). Petroleum Reservoir Rock and Fluid Properties. Boca Raton, FL: Taylor and Francis Group.

Dash, J.G., Fu, H. (1995). Wettlaufer, J.S., The Premelting of Ice and Its Environmental Consequences. Reports on Progress in Physics, 58, 115-167.

Decker, P.L. (2007) Brookian sequence stratigraphic correlations Umiat field to west central area to milne point field, west-central North Slope, Alaska: Alaska Division of Oil & Gas.

Freeze, R.A. (1994). Henry Darcy and the Fountains of Dijon. Ground Water, 32, 23–30.

Gates, G.L., Caraway, W.H. (1960). Well productivity related to drilling muds: Umiat field, Naval Petroleum Reserve No.4, Alaska. [Washington] U.S. Dept. of the Interior, Bureau of Mines.

Godabrelidze, V. (2010) Characterization and fluid flow properties of frozen rock systems of Umiat oil field, Alaska: Master's thesis, University of Alaska Fairbanks.

Ishizaki, T. (1995). Experimental study on unfrozen water migration in porous materials during freezing. Journal of Natural Disaster Science, 17, 65 –74.

Ishizaki, T., Maruyama, M., Furukawa, Y., Dash, J.G. (1996). Premelting of ice in porous silica glass. Journal of Crystal Growth, 1996, 162, 455 – 460.

Jensen, R.G., Shabad, T., Wrigh, A.W. (1983). (Eds.). Soviet Natural Resources in the World Economy. Chicago, IL: University of Chicago Press.

Johnson, E.F., Bossler, D.P. and Naumann, V.O. (1959). Calculation of relative permeability from displacement experiments. American Institute of Mining, Metallurgical, and Petroleum Engineers, 216, 370-372.

Johnson, O.L. (2010). Petrophysical property modeling of Umiat Field, a frozen oil reservoir: Master's thesis, University of Alaska Fairbanks.

Kleinberg, R.L., Flaum, C., Collett, T.S. (2004). Magnetic resonance log of Mallik 5L-38: hydrate saturation, growth habit, relative permeability and control of accumulation. In: Dallimore, S.R., Collett, T.S. (Eds.), Scientific Results from the Mallik 2002 Gas Hydrate Production Research Well, Mackenzie Delta, Northwest Territories, Canada. Geological Survey of Canada, Ottawa, Bulletin, 585.

Kleinberg, R.L., Griffin, D.D. (2005). NMR measurements of permafrost: unfrozen water assay, pore-scale distribution of ice, and hydraulic permeability of sediments. Cold Regions Science and Technology, 42, 63–77.

Kljucec, N.M, Yurkowski, K.J, Lipsett, L.R. (1974). Successful drilling of permafrost with a Bentonite–XC polymer, KCl mud system. The journal of Canadian Petroleum Technology, 01-05.

Konno, A., Izumiyama, K. (2002). Theory and modeling of interfacial tension force on the oil spreading under ice covers. Proceedings of the 16th IAHR International Symposium on Ice.

Kovarik, B. (2009). The oil reserve fallacy. Retrieved November 16, 2010 from http://www.radford.edu/wkovarik/oil/3unconventional.html

Kozeny, J. (1927). Ueber kapillare Leitung des Wassers im Boden. Sitzungsber Akad. Wiss., Wien, 136(2a), 271-306.

LePain, D.L, McCarthy, P.J., Kirkham, R. (2009). Sedimentology, stacking patterns, and depositional systems in the middle Albian-Cenomanian Nanushuk Formation in outcrop, central North Slope, Alaska. Division of Geological and Geophysical surveys.

Leverett, M.C. (1939). Flow of oil water mixtures through unconsolidated sands. American Institute of Mining, Metallurgical, and Petroleum Engineers, 132, 381-401.

Mraw, S.C., Naas-O'Rourke, D.F. (1979). Water in coal pores: low temperature heat capacity behavior of the moisture in Wyodak. Coal science, 205, 901–902.

Mull, C.G., Houseknecht, D.W., and Bird, K.J. (2003). Revised Cretaceous and Tertiary stratigraphic nomenclature in the Colville Basin, northern Alaska. U.S. Geological Survey Professional Paper, 1673, 51.

Musket, M. (1937). The Flow of Homogeneous Fluids through Porous Media. McGraw-Hill Book Company, New York.

Narahara, G.M., Pozzi, A.L. Jr., Blackshear, T.H. Jr. (1993). Effect of gas/oil relative permeabilities for water wet and mixed wet Berea rock. 114-122.

Øren, P., Bakke, S. (2003). Reconstruction of Berea sandstone and pore-scale modeling of wettability effects. Journal of Petroleum Science and Engineering, 39, 177–199.

Permafrost distribution in the Arctic. (2005). In UNEP/GRID-Arendal Maps and Graphics Library. Retrieved June 14, 2011 from http://maps.grida.no/go/graphic/permafrost-distribution-in-the-arctic.

Potter, C.J., Moore, C.J. (2003). Brookian structural plays in the National Petroleum Reserve, Alaska. U.S. Geological Survey.

Raymond, J. (1979) Steam water relative permeability. Doctor of Philosophy thesis, Stanford University.

Reed, M.A., Lovell, C.W., Altschaeffl, A.G., Wood, L.E. (1979). Frost–heaving rate predicted from pore-size distribution. Canadian Geotechnical Journal, 16, 463-472.

Sahoo, B.C., Vajjha, R.S., Ganguli, R., Chukwu, G.A., Das, D.K. (2009). Determination of Rheological Behavior of Aluminum Oxide Nanofluid and Development of New Viscosity Correlations. Petroleum Science and Technology, 27, 1757–1770.

Shen, P., Zhu, B., Li, X.B., Zhong, T., Wang, H. (2005). The influence of interfacial tension on water-oil two-phase relative permeability. Society of Core Analysts.

Tice, A.R., Oliphant, J.L., Nakano, Y., Jenkins, T.F. (1982). Relationship between the ice and unfrozen water phases in frozen soil as determined by pulsed nuclear magnetic resonance and physical desorption data. Cold Regions Research and Engineering Lab Report, 82-15.

Tsytovich, N.A. (1963). "Permafrost Problems," National Association of the USSR for Soil Mechanics and Foundation Engineering: 2nd Permafrost International Conference, 1963.

U.S. Energy Information Administration. (2005). Oil demand and supply forecast. Retrieved from November 16, 2010 from www.eia.gov.

Watanabe, K., Mizoguchi, M. (2002). Amount of unfrozen water in frozen porous media saturated with solution. Cold Regions Science and Technology, 34, 103-110.

Watt, J.S., Huckabay, A., Landt, M.R. (2010). Umiat: a North Slope giant primed for oil development. Oil & Gas Journal, 30-38.

Weatherford Laboratories. (2010). Water quality considerations resulting in the impaired injectivity of water injection and disposal wells. Retrieved March 3, 2011 from http://omnilabs.com/media/37365/water_quality_considerations.pdf.

Wilson, P.W., Arthur, J.W., Haymet, A.D.J. (1999). Ice Premelting during Differential Scanning Calorimetry: Biophysical Journal, 77, 2850–2855.

Wolfe, J. (2010). Freezing point depression and boiling point elevation: the effects of solutes and of pressure. Retrieved May 12 2011 from www.animations.physics.unsw.edu.au/jw/freezing-point-depression-boiling-point-elevation.htm.

Zhang, T., Barry, R.G., Knowles, K., Ling, F. (2003). Armstrong, R.L., Distribution of seasonally and perennially frozen ground in the Northern Hemisphere, in Permafrost. Phillips, Springman, and Arenson, eds. Swets and Zeitlinger

Appendix A

Permeability calculations were made using Darcy's Law (Equation 6).

$$Q = -\frac{kA\Delta P}{\mu L}$$

A.1 Calculations for Core 1:

Area of the Core sample = A = 10.471 cm^2
Volumetric flow rate of the fluid = Q = 0.05 cc/sec
Length of the sample = L = 15.24 cm

A.1.1 Absolute Permeability:

Viscosity of the water at room temperature = μ = 1.0002 cp
Pressure differential across the core = ΔP = 0.8 psi
Substituting all the respective values into Equation 6
Absolute permeability of Core 1 = 134.17md

A.1.2 Effective permeability of oil (core is saturated with Deionized water)

At 23°C:
Viscosity of oil at room temperature = μ = 1.04 cp
Pressure differential across the core = ΔP = 0.14psi
Substituting all the respective values into Equation 6
Effective permeability of oil = 81.1863md

At 0°C:
Viscosity of oil at room temperature = μ = 1.54 cp
Pressure differential across the core = ΔP = 0.24psi

Substituting all the respective values into Equation 6

Effective permeability of oil = 67.28md

At -5°C:

Viscosity of oil at room temperature = μ = 1.63 cp

Pressure differential across the core = ΔP = 0.36psi

Substituting all the respective values into Equation 6

Effective permeability of oil = 48.331md

At -10°C:

Viscosity of oil at room temperature = μ = 1.82 cp

Pressure differential across the core = ΔP = 0.42psi

Substituting all the respective values into Equation 6

Effective permeability of oil = 46.136md

A.1.3 Effective permeability of oil (core is saturated with Salinity 1)

At 23°C:

Viscosity of oil at room temperature = μ = 1.04 cp

Pressure differential across the core = ΔP = 0.12psi

Substituting all the respective values into Equation 6

Effective permeability of oil = 90.49md

At 0°C:

Viscosity of oil at room temperature = μ = 1.54 cp

Pressure differential across the core = ΔP = 0.19psi

Substituting all the respective values into Equation 6

Effective permeability of oil = 87.644md

At -5°C:

Viscosity of oil at room temperature = μ = 1.63 cp

Pressure differential across the core = ΔP = 0.23psi

Substituting all the respective values into Equation 6

Effective permeability of oil = 74.3802md

At -10°C:

Viscosity of oil at room temperature = μ = 1.82cp

Pressure differential across the core = ΔP = 0.32psi

Substituting all the respective values into Equation 6

Effective permeability of oil = 60.33md

A.1.4 Effective permeability of oil (core is saturated with Salinity 2)

At 23°C:

Viscosity of oil at room temperature = μ = 1.04 cp

Pressure differential across the core = ΔP = 0.13psi

Substituting all the respective values into Equation 6

Effective permeability of oil = 88.14md

At 0°C:

Viscosity of oil at room temperature = μ = 1.54 cp

Pressure differential across the core = ΔP = 0.19psi

Substituting all the respective values into Equation 6

Effective permeability of oil = 87.236md

At -5°C:

Viscosity of oil at room temperature = μ = 1.63 cp

Pressure differential across the core = ΔP = 0.26psi

Substituting all the respective values into Equation 6

Effective permeability of oil = 66.5079md

At -10°C:

Viscosity of oil at room temperature = μ = 1.82cp

Pressure differential across the core = ΔP = 0.35psi

Substituting all the respective values into Equation 6

Effective permeability of oil = 55.081md

A.2 Calculations for Core 2:

Area of the Core sample = A = 10.471 cm^2

Volumetric flow rate of the fluid = Q = 0.005 cc/min

Length of the sample = L = 15.24 cm

A.2.1 Absolute Permeability:

$$Q = -\frac{kA\Delta P}{\mu L} \quad (8)$$

Viscosity of the water at room temperature = μ = 1.0002 cp

Pressure differential across the core = ΔP = 0.7 psi

Substituting all the respective values into Equation 6

Absolute permeability of Core 2 = 153.342 md

A.2.2 Effective permeability of oil (core is saturated with Deionized water)

At 23°C:

Viscosity of oil at room temperature = μ = 1.04 cp

Pressure differential across the core = ΔP = 0.13psi

Substituting all the respective values into Equation 6

Effective permeability of oil = 87.2 md

At 0°C:

Viscosity of oil at room temperature = μ = 1.54 cp

Pressure differential across the core = ΔP = 0.21psi

Substituting all the respective values into Equation 6

Effective permeability of oil = 79.8815md

At -5°C:

Viscosity of oil at room temperature = μ = 1.63 cp

Pressure differential across the Core = ΔP = 0.35psi

Substituting all the respective values into Equation 6

Effective permeability of oil = 49.5md

At -10°C:

Viscosity of oil at room temperature = μ = 1.82 cp

Pressure differential across the core = ΔP = 0.4psi

Substituting all the respective values into Equation 6

Effective permeability of oil = 48.04md

A.2.3 Effective permeability of oil (core is saturated with Salinity 1)

At 23°C:

Viscosity of oil at room temperature = μ = 1.04 cp

Pressure differential across the core = ΔP = 0.12psi

Substituting all the respective values into Equation 6

Effective permeability of oil = 93.169md

At 0°C:

Viscosity of oil at room temperature = μ = 1.54 cp

Pressure differential across the core = ΔP = 0.2psi

Substituting all the respective values into Equation 6

Effective permeability of oil = 82.5md

At -5°C:

Viscosity of oil at room temperature = μ = 1.63 cp

Pressure differential across the core = ΔP = 0.23psi

Substituting all the respective values into Equation 6

Effective permeability of oil 2 = 77.26md

At -10°C:

Viscosity of oil at room temperature = μ = 1.82cp

Pressure differential across the core = ΔP = 0.31psi

Substituting all the respective values into Equation 6

Effective permeability of oil = 63.59 md

A.2.4 Effective permeability of oil (core is saturated with Salinity 2)

At 23°C:

Viscosity of oil at room temperature = μ = 1.04 cp

Pressure differential across the core = ΔP = 0.12psi

Substituting all the respective values into Equation 6

Effective permeability of oil = 89.9106md

At 0°C:

Viscosity of oil at room temperature = μ = 1.54 cp

Pressure differential across the core = ΔP = 0.2psi

Substituting all the respective values into Equation 6

Effective permeability of oil = 83.692 md

At -5°C:

Viscosity of oil at room temperature = μ = 1.63 cp

Pressure differential across the core = ΔP = 0.23psi

Substituting all the respective values into Equation 6

Effective permeability of oil = 75.60 md

At -10°C:

Viscosity of oil at room temperature = μ = 1.82cp

Pressure differential across the core = ΔP = 0.33 psi

Substituting all the respective values into Equation 6

Effective permeability of oil = 59.73 m

Appendix B

Shear stress (d/cm^2) vs shear strain (1/sec) values were plotted at each temperature from 23°C to -10°C. The slope of the straight line obtained from that respective graph gives the viscosity of the fluid at that particular temperature. Values of viscosity at different temperatures were plotted and are shown in this section. Figure B.1 shows the viscosity trend with respect to temperature until -5°C. Viscosity measurements failed for water samples at -10°C due to freezing.

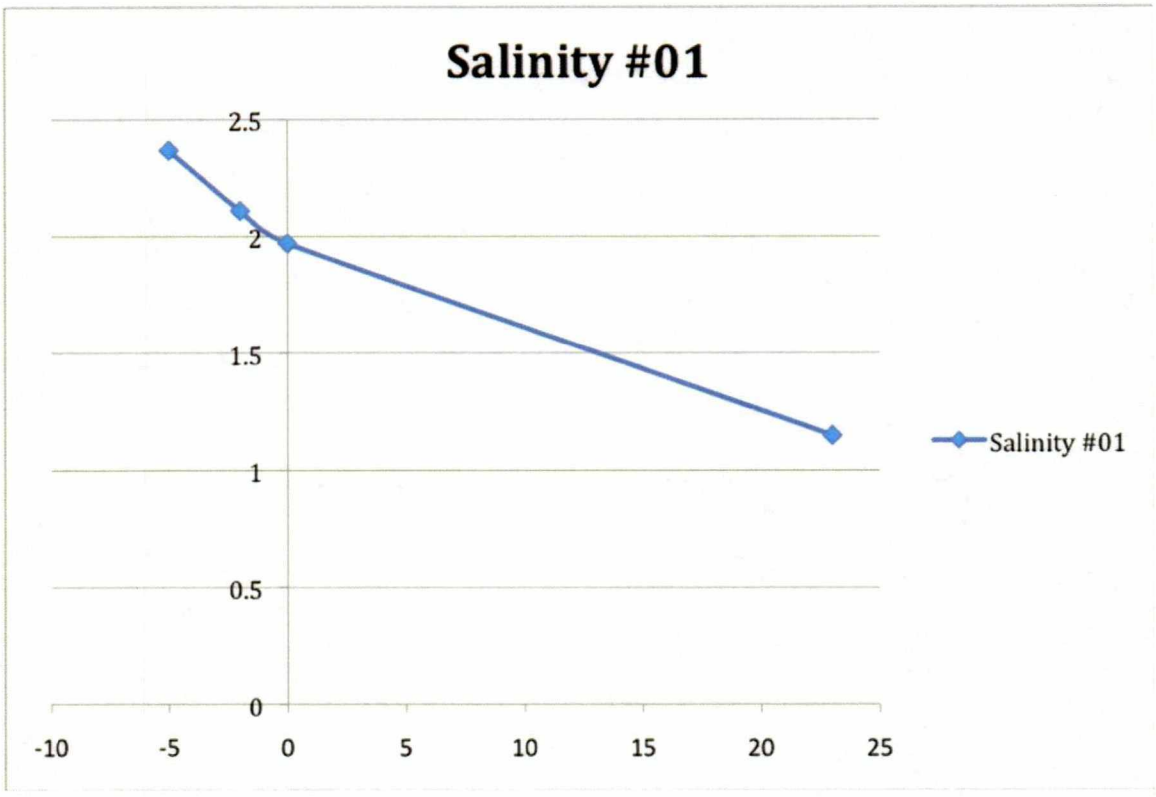

Figure B.1: Viscosity vs Temperature profile for Salinity 1

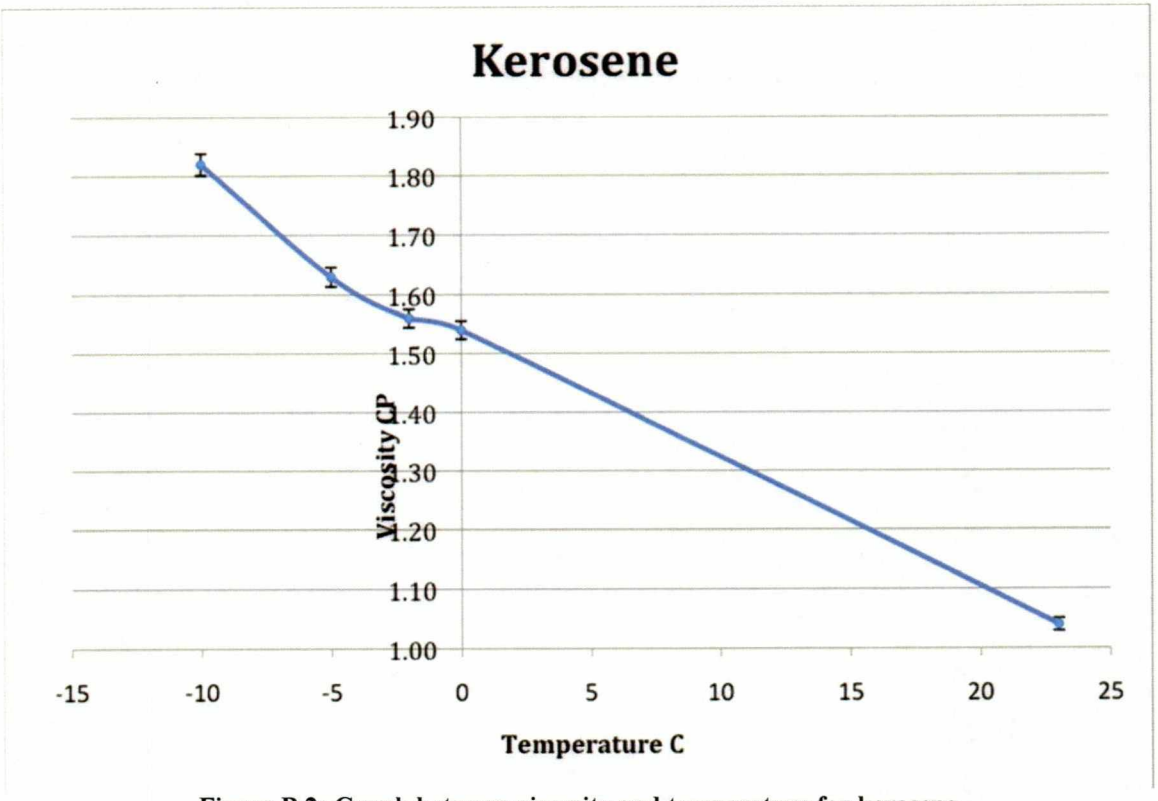

Figure B.2: Graph between viscosity and temperature for kerosene

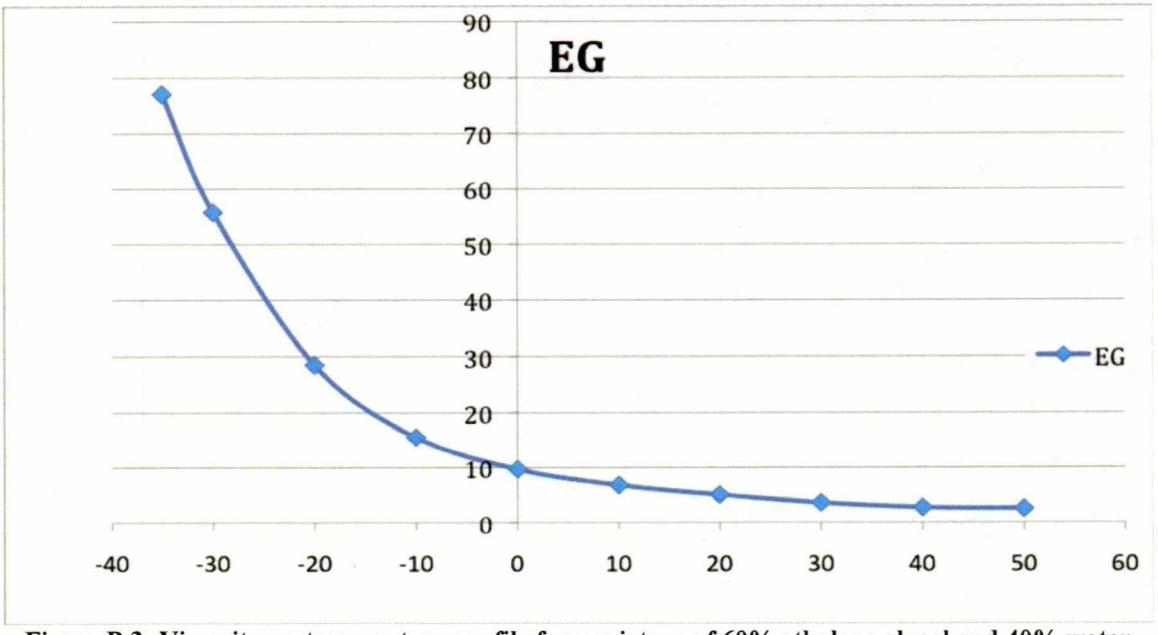

Figure B.3: Viscosity vs. temperature profile for a mixture of 60% ethylene glycol and 40% water

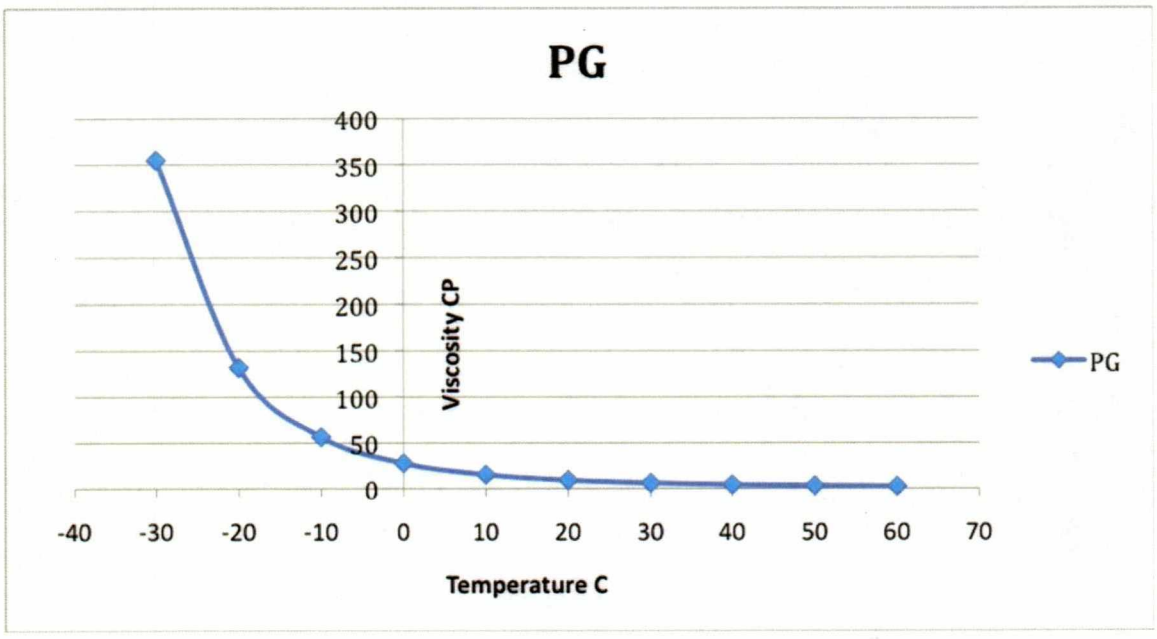

Figure B.4: Viscosity vs temperature profile for a mixture of 60% propylene glycol and 40% water

Appendix C

Volumetric average radius of the pore (b) from capillary measurements was calculated as 1.60μm. This value was used in alternative Kozeny–Carman Equation for the calculation of radius of ice kernel that is formed at the center of the pore. Alternative KC Equation was given as

$$k = -\frac{\phi}{8\tau^2} b^2 \left[1 + \frac{a^2}{b^2} + \left(1 - \frac{a^2}{b^2} \right) \frac{1}{\ln(a/b)} \right] \quad (41)$$

Calculation of 'a' for DI water at -10°C:

From Section 4.1, Assumption 2 implies that

$(\frac{\phi}{8\tau^2} b^2)$ = 81.1863 md; b = 1.35 μm; k= 46.136 md at -10°C.

Substituting the above values in Equation 41

$$46.136 = 81.1863 \left[1 + \frac{a^2}{(1.35)^2} + \left(1 - \frac{a^2}{(1.35)^2} \right) \frac{1}{\ln(a/1.35)} \right]$$

By solving the above Equation using Microsoft Excel, radius of ice formed (a) at -10°C was calculated as 0.145 μm.

Calculation of 'a' for Salinity 2at -10°C:

$(\frac{\phi}{8\tau^2} b^2)$ = 88.14 md; b = 1.35 μm; k= 55.081 md at -10°C.

Substituting the above values in Equation 41

$$55.081 = 88.14 \left[1 + \frac{a^2}{(1.35)^2} + \left(1 - \frac{a^2}{(1.35)^2} \right) \frac{1}{\ln(a/1.35)} \right]$$

By solving the above Equation using Microsoft Excel, radius of ice formed (a) at -10°C was calculated as 0.098 μm.

Calculation of 'a' for Salinity 1 at -10°C:

$(\frac{\phi}{8\tau^2}b^2)$ = 90.49 md; b = 1.35 μm; k= 60.33 md at -10°C.

Substituting the above values in Equation 41

$$60.33 = 90.49\left[1+\frac{a^2}{(1.35)^2}+\left(1-\frac{a^2}{(1.35)^2}\right)\frac{1}{\ln\left(a/1.35\right)}\right]$$

By solving the above Equation using Microsoft Excel, radius of ice formed (a) at -10°C was calculated as 0.069 μm.